On-board electric powertrain control for the compensation of the longitudinal acceleration oscillations caused by road irregularities

Mechanism and Machine Theory 202 (2024) 105759

Contents lists available at ScienceDirect

Mechanism and Machine Theory

journal homepage: www.elsevier.com/locate/mechmt

Research paper

On-board electric powertrain control for the compensation of the longitudinal acceleration oscillations caused by road irregularities

Pietro Stano [a], Davide Lazzarini [a,b,c], Silvio Santoro [a,b], Mario Mihalkov [a], Umberto Montanaro [a], Alessandro Vigliani [b], Antonella Ferrara [c], Miguel Dhaens [d], Aldo Sorniotti [b,*]

[a] School of Mechanical Engineering Sciences, University of Surrey, GU2 7XH, Guildford, UK
[b] Department of Mechanical and Aerospace Engineering (DIMEAS), Department of Electronics and Telecommunications (DET), Politecnico di Torino, 10129 Turin, Italy
[c] Department of Electrical, Computer and Biomedical Engineering, University of Pavia, 27100 Pavia, Italy
[d] Tenneco Automotive, 3800 Sint-Truiden, Belgium

ARTICLE INFO

Keywords:
Nonlinear model predictive control
On-board powertrains
Longitudinal vibration control
Road irregularity

ABSTRACT

Road irregularities affect vehicle comfort by causing vertical and longitudinal acceleration oscillations. While the current ride comfort enhancement solutions are based on the compensation of the vertical acceleration of the sprung mass, the compensation of the longitudinal dynamics excited by road irregularities has been successfully explored only for in-wheel powertrains. The scope of this study is to demonstrate that also on-board electric powertrains with torsional dynamics of the half-shafts have the potential for effective compensation, thanks to the road profile preview. This paper presents a proof-of-concept nonlinear model predictive controller (NMPC) with road preview, which is assessed with a validated simulation model of an all-wheel drive electric vehicle. Three powertrain layouts are considered, with four in-wheel, four on-board, and two on-board electric machines. The control function is evaluated along multiple manoeuvres, through comfort-related key performance indicators (KPIs) that, for the four on-board layout along a road step test at 40 km/h, highlight >80% improvements. Finally, the real-time implementability of the algorithms is demonstrated, and preliminary experiments are conducted on an electric quadricycle prototype, with more than halved oscillations of the relevant variables.

1. Introduction

Vehicle drivability describes the complex interactions between the driver and the vehicle regarding the longitudinal acceleration aspects in terms of vibration transmissibility and fast response to driver inputs, and therefore relates to the perceived safety and comfort [1]. Road irregularities play a key role in ride comfort, as they involve undesirable variations in the magnitude and direction of the force applied to the rolling wheel [2,3]. Such tyre force vibrations are transmitted to the unsprung mass, and then to the sprung mass, through the suspension arms and bushings, as explained in [4–6], which causes vertical and longitudinal accelerations of the unsprung and sprung masses [7]. While extensive literature deals with the attenuation of the effect of road irregularities on the vertical sprung mass acceleration by means of active and semiactive suspension controllers [8–11], the longitudinal acceleration component

* Corresponding author.
E-mail address: aldo.sorniotti@polito.it (A. Sorniotti).

https://doi.org/10.1016/j.mechmachtheory.2024.105759
Received 27 June 2024; Received in revised form 1 August 2024; Accepted 2 August 2024
Available online 29 August 2024

List of Symbols

$a,\ b$	Front and rear semi-wheelbases
$a_1,\ b_{1/2}, c_{1/2}, d_{1/2}$	Constant tuneable coefficients of the vertical suspension force of the shock absorbers
$a_c,\ b_c$	Horizontal and vertical semi-axes of the ellipses of the enveloping model
A_{car}	Frontal area of the vehicle
a_d	Shape factor of the exponential function expressing the stiffness and damping contributions of the half-shaft torque
c	Ellipse shape parameter of the tyre enveloping model
C_d	Aerodynamic drag coefficient
$c_{hs,ij}$	Equivalent torsional damping of the half-shafts
$c_{r,i}$	Radial damping coefficient of the tyre
$c_{t,i}$	Tangential damping coefficient of the tyre
$c_{x,i}$	Longitudinal damping coefficient of the suspension
d_{i_e}	Bottom profile of the i_e ellipse of the enveloping model
$f_{1,exp,ij},\ f_{2,exp,ij}$	Exponential functions in the stiffness and damping contributions of the half-shaft torque
$f_{1,ij},\ f_{2,ij}$	Switching functions for the stiffness and damping contributions of the half-shaft torque
$f_{a,ij},\ f_{b,ij}$	Linear functions in the stiffness contribution of the half-shaft torque
$f_{c,ij}$	Linear function in the damping contribution of the half-shaft torque
$F_{c,x,ij}$	Damping force contribution of the suspension bushings
$F_{c,z,ij}$	Vertical suspension force caused by the shock absorber
$f_d()$	Prediction model function
F_{drag}	Aerodynamic drag force
$F_{k,x,ij}$	Stiffness force contribution of the suspension bushings
$F_{k,z,ij}$	Vertical suspension force of the spring
$F_{r,ij}$	Radial force related to the tyre structure behaviour
$F_{r,x,ij},\ F_{r,z,ij}$	Longitudinal and vertical components of the radial force related to the tyre structure behaviour
$f_{roll},\ f_{roll,0},\ f_{roll,2}$	Rolling resistance coefficients
$F_{roll,i}$	Rolling resistance force
$F_{t,ij}$	Tangential force related to the tyre structure behaviour
$F_{t,x,ij},\ F_{t,z,ij}$	Longitudinal and vertical components of the tangential force related to the tyre structure behaviour
$F_{x,ij}$	Traction/braking tyre force
$F_{x,x,ij},\ F_{x,z,ij}$	Longitudinal and vertical components of the traction/braking tyre force
$F_{z,ap,ij}$	Longitudinal load transfer contribution of the unsprung mass caused by the suspension anti-properties
$F_{z,b,i}$	Equivalent vertical force of the sprung mass associated with the suspension anti-properties
$F_{z,b,ij}$	Equivalent sprung mass force of the individual corner associated with the suspension anti-properties
g	Gravitational acceleration
$g_d()$	System output function
h_g	Centre of gravity height
$i = F,R$	Index or subscript indicating the front or rear axles
$i_e = F,R$	Index or subscript indicating the front or rear ellipses
i_p	Transmission ratio between the side gears and planetary gears of the differential
i_t	Transmission gear ratio
J	Cost function
$j = L/R$	Index or subscript indicating the left or right sides
j_c	Initial time step of the prediction within the nonlinear optimal control problem
$J_{hs,ij}$	Mass moment of inertia of the half-shaft
$J_{eq,1,i}\ ,\ J_{eq,2,i}$	Equivalent mass moment of inertia of the front drivetrain
$J_{eq,ij}$	Equivalent mass moment of inertia of the drivetrain for the '4 on-board' configuration
J_m	Mass moment of inertia of the rotor of the electric motor (EM)
$J_{mgd,i}$	Equivalent mass moment of inertia of the rotating parts of the motor, gearbox and differential case
$J_{p,i}$	Mass moment of inertia of the planetary gears
$J_{s,i}$	Mass moment of inertia of the side gears
J_{stage}	Stage cost contribution
$J_{terminal}$	Terminal cost contribution
$J_{u,y,i}$	Mass moment of inertia of the rotating parts of the unsprung mass of the individual corner
J_{WT}	Weight tuning cost function
k	Discretisation step along the prediction horizon
$k_{hs,ij}$	Equivalent torsional stiffness of the half-shafts

$k_{r,i}$	Radial stiffness of the tyre
$k_{t,i}$	Tangential stiffness of the tyre
$k_{x,i}$	Longitudinal suspension stiffness
$k_{z,i}$	Vertical suspension stiffness
Lb_{T_m}, Ub_{T_m}	Lower and upper motor torque limits
l_s	Relative horizontal distance between the cams of the enveloping model
$m_{app,i}$	Apparent mass used in the prediction model of the '2 on-board' configuration
$m_{app,ij}$	Apparent mass used in the prediction model of the '4 on-board' and 'In-wheel' configurations
m_b	Sprung mass
m_m	Individual EM mass
$M_{roll,ij}$	Rolling resistance moment
m_{tot}	Total vehicle mass
$m_{u,i}$	Unsprung mass of the individual corner
N_h	Number of steps of the prediction horizon
N_{iter}	Number of solver iterations
N_p	Number of steps of the preview horizon
P_0	Effective road profile position of the enveloping model
p_{ij}	Parameter vector
p_k	Parameter or external disturbance vector
p_T	Front-to-total anti-properties distribution factor
Q, Q_i, Q_{ij}	Weight matrices of the stage cost on the system outputs
Q_{max}, Q_{min}	Matrices including the maximum and minimum values of the stage cost weights on the system outputs
Q_t, $Q_{t,i}$, $Q_{t,ij}$	Weight matrices of the terminal cost on the system outputs
R, R_i, R_{ij}	Weight matrices on the control inputs
$R_{lad,ij}$	Laden wheel radius
R_{max}, R_{min}	Matrices including the maximum and minimum values of the cost function weights on the control inputs
$RMS_{\dddot{x}_b}$	Root mean square error value of the longitudinal jerk of the vehicle
$RMS_{\ddot{x}_b}$	Root mean square error value of the longitudinal vehicle acceleration with respect to (w.r.t.) its steady-state reference
$R_{roll,i}$	Rolling wheel radius
t_h	Prediction horizon
$T_{hs,c,ij}$	Damping contribution of the half-shaft torque
$T_{hs,ij}$	Half-shaft torque
$T_{hs,k,ij}$	Stiffness contribution of the half-shaft torque
$T_{hs,req,ij}$	Requested half-shaft torque
$T_{m,corr,i}$, $T_{m,corr,ij}$	Corrected motor torque
$T_{m,i}, \dot{T}_{m,i}$	Electro-magnetic EM torque and its time derivative for the '2 on-board' configuration
$T_{m,ij}$, $\dot{T}_{m,ij}$	Electro-magnetic EM torque and its time derivative for the '4 on-board' configuration
$T_{m,max}$, $T_{m,min}$	Maximum and minimum values of the EM torque
$T_{m,req,i}$, $T_{m,req,ij}$	Reference EM torque
t_p	Preview time
t_s	Sampling time
$T_{w,req,ij}$	Reference wheel torque
U	Control input sequence
u_k	Control input at the k-th optimal control problem step
u_{max}, u_{min}	Upper and lower bounds of the control actions
$VDV_{\ddot{x}_b}$	Fourth power longitudinal acceleration vibration dose value
$w_{1,WT}$	Weight tuning cost function weight associated with $RMS_{\dddot{x}_b}$
$w_{2,WT}$	Weight tuning cost function weight associated with $VDV_{\ddot{x}_b}$
W_{ij}	Equivalent road displacement
$w_{ij}, \dot{w}_{ij}$	Effective road height of the enveloping model and its time derivative
x	State vector
x_0	Initial states of the nonlinear optimal control problem (OCP)
x_b, $\dot{x}_b, \ddot{x}_b$	Longitudinal displacement, speed and acceleration of the sprung mass
$\dot{x}_{b,in}$	Initial vehicle speed
x_{e,i_e}, z_{e,i_e}	Longitudinal and vertical position of the i_e ellipse of the enveloping model
x_{in}	Initial value of the state vector
$x_u, \dot{x}_u, \ddot{x}_u$	Longitudinal displacement, speed and acceleration of the unsprung mass
$z_b, \dot{z}_b, \ddot{z}_b$	Vertical displacement, speed and acceleration of the sprung mass
Z_{e,i_e}	Vertical coordinates of the centre of the cam of the enveloping model in the global reference system

z_k	Predicted outputs along the prediction horizon
z_{N_h}	Terminal value of the predicted outputs
z_r	Road height
z_{ref,N_h}	Terminal value of the reference outputs
$z_{ref,k}$	Value of the reference outputs along the prediction horizon
$z_u, \dot{z}_u, \ddot{z}_u$	Vertical displacement, speed and acceleration of the unsprung mass
α	Half of the equivalent torsional backlash of the half-shafts
B_{ij}	Equivalent road gradient
$\beta_{y,ij}$	Effective road slope of the enveloping model
$\Delta J_{hs,i}$	Difference between the mass moments of inertia of the right and left half-shafts
ΔT_m	Motor torque correction
$\Delta \ddot{x}_{b,\max}$	Maximum longitudinal acceleration error
Δx_r	Longitudinal distance corresponding to the asymmetry in the step road profile application
$\Delta\dot{\theta}_{s,i}, \Delta\ddot{\theta}_{s,i}$	Angular speed and acceleration difference between the side gears
η_t	Transmission efficiency
$\dot{\theta}_{df}, \ddot{\theta}_{df}$	Angular speed and acceleration of the differential case
$\theta_s, \dot{\theta}_s, \ddot{\theta}_s$	Angular half-shaft displacement, speed and acceleration
$\theta_u, \dot{\theta}_u, \ddot{\theta}_u$	Angular wheel displacement, speed and acceleration
ρ_{air}	Air density
τ_m	EM time constant
ϕ_{ij}	Angle associated with the suspension arm, related to the suspension anti-property coefficient

and related compensation strategies are rarely mentioned. Although smaller than the vertical acceleration oscillations, the longitudinal acceleration dynamics are not negligible, and have significant impact on comfort [12].

Because of their slow dynamics, internal combustion engines cannot quickly adjust the torque to counteract the effects of rough roads. However, electric powertrains, in both their in-wheel and on-board set-ups, offer more responsive and accurate wheel torque control performance [13]. In this respect, shaft-less drivetrains, i.e., with in-wheel machines, are the optimal solution, as they are not subject to any form of torsional dynamics. This improves the performance of wheel slip and direct yaw moment controllers [14,15]. Nevertheless, a certain amount of vibration due to the electro-mechanical/magnetic coupling is inevitable during torque generation [16–18]. The torque ripple of in-wheel machines, which is directly transmitted to the wheels, can also affect comfort on smooth road surfaces [19,20], and can be attenuated through appropriate electric motor (EM) designs or control strategies [21–23]. In addition to the vibration aspects of in-wheel machines, described in [24], the associated increase in the unsprung mass can result in a ride comfort and road holding decay [25–28].

Only a few authors have discussed the option of using the powertrain torque to smoothen the longitudinal acceleration oscillations excited by road irregularities, and all the applications are limited to internal combustion engines or in-wheel motors. In Bakirci et al. in [29], the use of a proportional integral controller brings negligible benefit, due to the slow internal combustion engine response. In [30], Fukudome presents a proportional controller based on the difference in longitudinal speed between the unsprung and sprung masses in a vehicle with in-wheel powertrains. In [31] and [32], Walz et al. propose a feedforward controller that reduces the longitudinal acceleration oscillation over a known step-like road profile, only at less than 10 km/h of vehicle speed. A controller consisting

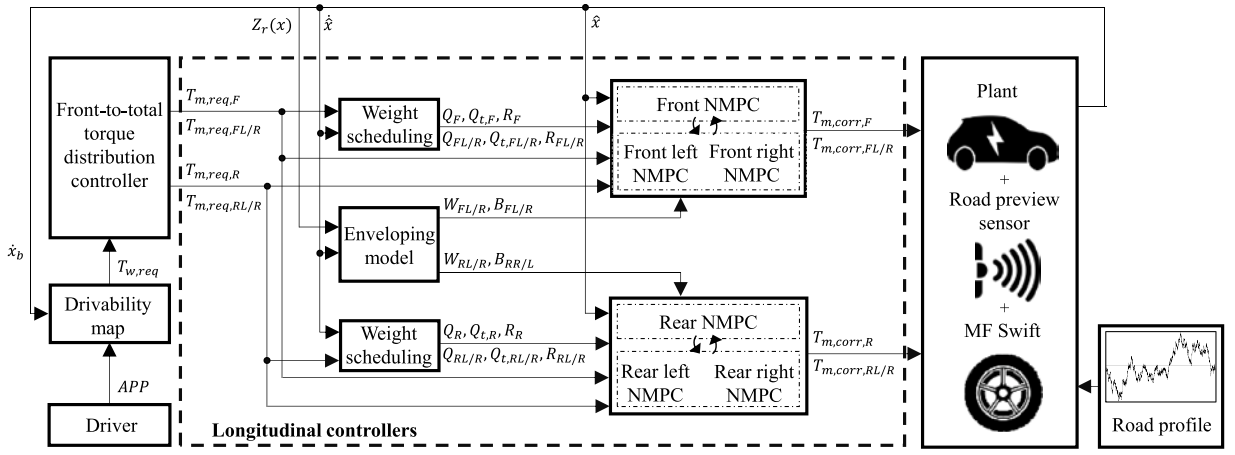

Fig. 1. Simplified schematic of the simulation and control environment for the three considered cases.

of feedforward and feedback contributions is proposed in [33], tuned through the model in [6], and experimentally validated in [34]. Neither control contribution considers the current or expected road profile. The feedforward contribution is based on the longitudinal acceleration demand and an inverse vehicle model. The feedback term includes a deadtime compensator observer to provide robustness against communications delays. A promising methodology to enhance performance is represented by controller formulations considering the preview information on the road profile ahead, which is already successfully used in production vehicles for the operation of controlled suspension systems [35,11]. In this respect, the previous work of our research team [36] includes a nonlinear model predictive controller (NMPC) of the longitudinal vehicle dynamics, based on the road profile preview, for electric vehicles (EVs) with in-wheel motors. The results highlight that in-wheel powertrains, in conjunction with the knowledge of the road irregularities ahead, can significantly reduce the longitudinal acceleration oscillations compared to benchmarking controllers, such as the one in [30].

In summary, the compensation of the longitudinal vehicle dynamics induced by irregular roads has not been explored for the case of on-board electric powertrains yet, in which the powertrain is part of the EV sprung mass. Since on-board solutions currently cover almost the entire EV market, this is an important gap from the practical perspective. The reason is the complex torsional dynamics caused by the half-shafts [37], and accentuated by the backlash in the transmission gears and driveline components [38,39]. Despite the drivetrain dynamics can be attenuated by the anti-jerk controllers [40], they significantly affect the responsiveness and accuracy of any wheel torque control algorithm, including the road preview controller in [36], whose prediction model considers the EM speed to be the same as the wheel speed, and therefore is suitable only for in-wheel powertrain applications.

The scope of this study is to demonstrate that it is possible to achieve a significant attenuation of the longitudinal acceleration oscillations caused by road irregularities also in case of on-board powertrains, by using NMPC algorithms concurrently embedding road preview and consideration of the drivetrains dynamics. To this purpose, novel proof-of-concept NMPC formulations are presented and evaluated for three four-wheel-drive EV architectures, including: i) four in-wheel direct drive EMs, referred to as 'In-wheel' in the remainder, where the EMs are part of the unsprung mass; ii) four on-board powertrains, referred to as '4 on-board', where the individual EMs are mounted on the chassis, and connected to the respective wheel through a single-speed transmission system, outer and inner constant velocity joints, and a half-shaft; and iii) two on-board – one per axle – EMs, connected to the wheels through a single-speed gearbox and an open mechanical differential ('2 on-board').

The remainder is organized as follows: Section 2 describes the simulation environment; Section 3 deals with the novel NMPC formulations; Section 4 discusses the selected road profiles and performance indicators; Section 5 analyses the simulation results; Section 6 presents the real-time implementations and proof-of-concept experiments; finally, Section 7 summarises the main conclusions.

2. Simulation and control environment

2.1. Simulation and control architecture

The simulation and control environment is reported in Fig. 1, and includes:

- The driver model, which, in the context of the purely longitudinal dynamics analyses of this study, defines the accelerator pedal position, *APP*.
- The drivability map, which computes the reference wheel torque at the EV level, $T_{w,req}$, as a function of *APP* and vehicle speed.

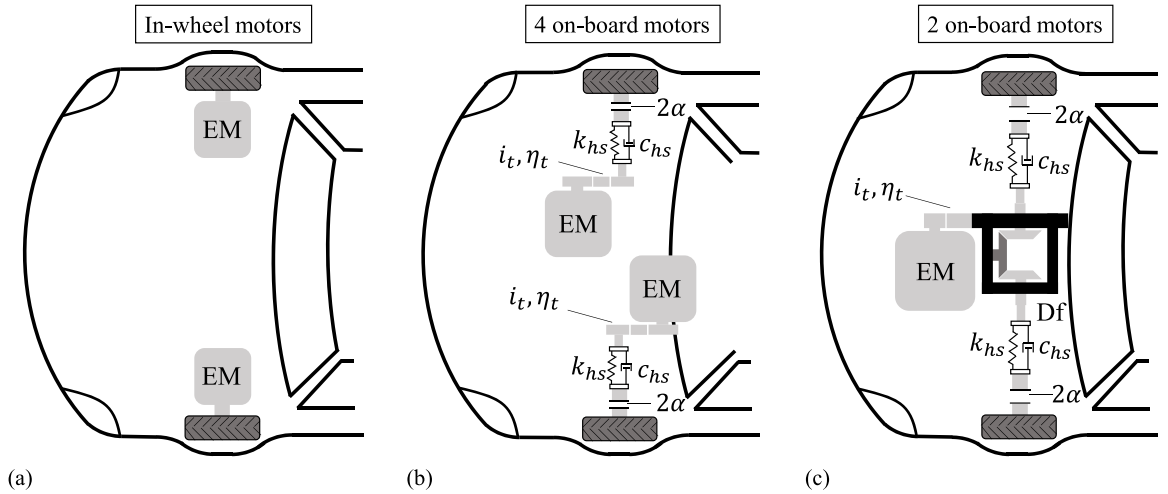

Fig. 2. Considered EV powertrain architectures: (a) 'In-wheel'; (b) '4 on-board'; and (c) '2 on-board'.

- The front-to-total torque distribution controller, which determines, based on drivability, vehicle dynamics and powertrain efficiency requirements, the individual reference motor torque values, $T_{m,req,i}$, for the '2 on-board' case, or $T_{m,req,ij}$ for the 'In-wheel' or '4 on-board' configurations, where the subscript i indicates the front (F) or rear (R) axle, and j refers to the left (L) or right (R) vehicle side. In the specific implementation, given the focus on the dynamic compensation of the longitudinal acceleration oscillations induced by road irregularities, a 50:50 reference front-to-rear motor torque distribution was selected for simplicity, since – in case of identical front and rear powertrains – such torque ratio is energy-efficient for a broad range of operating conditions, see the analyses in [41] and [42]. Future studies will generalise the assessment of the proposed controllers for varying torque distribution conditions.
- The longitudinal controllers, which are the focus of the analysis, and consist of: i) the enveloping model, which approximates the tyre filtering capability when rolling over irregular roads. Starting from the vector of the vertical displacement of the road ahead in points discretised according the NMPC prediction horizon, resulting from the road scanning sensor measurements, the enveloping model provides the corresponding vectors with the equivalent road displacement, W_{ij}, and road gradient, B_{ij}, at the considered corner; ii) two or four NMPC algorithms – one per EM – based on the considered powertrain architectures, according to a distributed control approach. In fact, when the '2 on-board' case is selected, two controllers, one per axle, provide the corrected EM torque, $T_{m,corr,i}$, which corresponds to the 'Front NMPC' and 'Rear NMPC' blocks in Fig. 1. Vice versa, when the 'In-wheel' or '4 on-board' configurations are selected, four controllers, one per EV corner, provide the modified EM torque, $T_{m,corr,ij}$, see the grey NMPC blocks in Fig. 1; and iii) weight scheduling blocks, which select the optimal NMPC cost function weights, Q_i or Q_{ij}, $Q_{t,i}$ or $Q_{t,ij}$, and R_i or R_{ij}, depending on the current operating conditions, e.g., in terms of vehicle speed, driving torque, and road profile ahead.
- The high-fidelity nonlinear vehicle model for control system assessment. The longitudinal vehicle dynamics model, implemented in Matlab/Simulink, includes 15 degrees of freedom, i.e., the longitudinal, vertical, and rotational dynamics of each unsprung mass, and the longitudinal, vertical, and pitch dynamics of the sprung mass. The nonlinearities of suspension springs and dampers, as well as the compliance properties of the suspension bushings, which are especially relevant in the longitudinal direction, are also considered for the specific controller assessment. A transfer function formulation simulates the electromagnetic EM torque

Table 1
Main vehicle and drivetrain parameters for the considered configurations.

Parameter	Symbol	Value	Unit
Front semi-wheelbase	a	1.473	[m]
Rear semi-wheelbase	b	1.455	[m]
Centre of gravity height	h_g	0.631	[m]
Aerodynamic drag coefficient	C_d	0.28	[-]
Frontal area	A_{car}	2.65	[m^2]
In-wheel			
Sprung mass	m_b	2593	[kg]
Unsprung mass of the individual corner	$m_{u,F/R}$	65	[kg]
Mass moment of inertia of the rotating parts of the unsprung mass of the individual corner	$J_{u,y,F/R}$	1.60	[kgm^2]
Individual EM mass	m_m	35	[kg]
EM time constant	τ_m	5.7	[ms]
EM rotor inertia	J_m	0.210	[kgm^2]
Maximum EM torque	$T_{m,max}$	1500	[Nm]
4 on-board			
Sprung mass	m_b	2789	[kg]
Unsprung mass of the individual corner	$m_{u,F/R}$	30	[kg]
Mass moment of inertia of the rotating parts of the unsprung mass of the individual corner	$J_{u,y,F/R}$	1.39	[kgm^2]
Equivalent gear ratio of the mechanical transmission	i_t	4.5	[-]
Equivalent transmission efficiency	η_t	0.96	[-]
Equivalent transmission backlash referred to the wheels	2α	1.26	[deg]
Individual EM mass	m_m	49	[kg]
EM time constant	τ_m	5.7	[ms]
EM rotor inertia	J_m	0.067	[kgm^2]
Maximum EM torque	$T_{m,max}$	350	[Nm]
2 on-board			
Sprung mass	m_b	2707	[kg]
Unsprung mass of the individual corner	$m_{u,F/R}$	30	[kg]
Mass moment of inertia of the rotating parts of the unsprung mass of the individual corner	$J_{u,y,F/R}$	1.39	[kgm^2]
Equivalent gear ratio of the mechanical transmission	i_t	8.0	[-]
Equivalent transmission efficiency	η_t	0.96	[-]
Equivalent transmission backlash referred to the wheels	2α	3.44	[deg]
Individual EM mass	m_m	57	[kg]
EM time constant	τ_m	25	[ms]
EM rotor inertia	J_m	0.086	[kgm^2]
Maximum EM torque	$T_{m,max}$	400	[Nm]

dynamics. The drivetrain model varies depending on the selected configuration, and includes the torsional dynamics of the relevant components, e.g., half-shafts when present, and the driveline backlash [43]. An extensively experimentally validated semi-empirical tyre model for ride comfort analysis, i.e., MF-Swift [44], has been interfaced with the vehicle model. MF-Swift conjugates the Pacejka magic formula model for tangential tyre force computation, with appropriate enveloping and tyre structure model. In particular, the rigid ring option was selected for the simulations of the study, which adds 6 degrees of freedom for each tyre, and describes the primary vibration modes of the tyre belt. These features enable accurate, fast and robust tyre-road contact force and moment simulations for frequencies up to ~100 Hz. During the simulation activity, it was verified that the effect of the EM torque ripple is negligible, to the purpose of assessing the proposed algorithms, see also [40].

2.2. Case study electric vehicle configurations

The case study EV of the simulations of this study is a sport utility vehicle, used as one of the demonstrators of the European Horizon 2020 EVC1000 project [45]. In the remainder, the same EV is simulated with the drivetrain architectures in Fig. 2, where, for clarity of representation, only the front axle is shown, since the rear one is identical. For the on-board powertrain configurations, the notations i_t and η_t denote the transmission gear ratio and efficiency; k_{hs} and c_{hs} refer to the equivalent torsional stiffness and damping values of the half-shafts; and the backlash parameter α is the half of the equivalent torsional clearance between the mating drivetrain components. The nominal values of the main vehicle parameters for the different powertrain configurations are summarized in Table 1. The in-wheel EM parameters are from the plate data of units considered within EVC1000, while the powertrain parameters for '4 on-board' and '2 on-board' are from the datasheets of the production units HVH250-090 and HVH250-115 by Cascadia Motion. As '2 on-board' also includes the open differential model, a greater equivalent backlash is considered with respect to (w.r.t.) the '4 on-board' layout.

The baseline version of the considered EV, i.e., with one independent on-board motor per axle, was equipped with: a) four monoaxial accelerometers to measure the vertical acceleration of the unsprung masses; b) four 3-axis accelerometers installed on the sprung mass at each corner of the vehicle; and c) a 3-axis gyroscope to capture the accelerations and angular velocities of the sprung mass. All the sensors are from the Bosch Motorsport series. This setup was experimentally tested on a standard ride comfort road, as shown in Fig. 3. The time domain results were converted into the frequency domain, and are expressed in terms of power spectral densities (PSDs) in Fig. 4, which reports the measured vertical and longitudinal accelerations of the sprung mass, in proximity of one of the front suspension strut attachments, as well as the corresponding and well-matching profiles from the high-fidelity vehicle model. The in-wheel powertrain dynamics are those experimentally validated on an EM test rig in [36]. The on-board drivetrain model embedded in the high-fidelity model is the same presented by Scamarcio et al. in [46], which has been experimentally validated along tip-in manoeuvres, for multiple initial vehicle speeds and torque demands (see the original paper for the validation plots).

To highlight the different dynamic response of the nominal parametrisations of the three considered drivetrain configurations, Fig. 5 reports the simulated time profiles of the longitudinal acceleration along a tip-in / tip-out test [47], implying positive and negative steps of torque demand, $T_{w,req,ij}$, at each wheel, with a 1500 Nm amplitude. Because of its greater EM time constant and equivalent backlash, '2 on-board' exhibits the slowest time response. On the other end of the spectrum, 'In-wheel', thanks to the smaller time constant of its electric machines as well as its shaft-less architecture, i.e., without transmission backlash and torsional dynamics, exhibits the most reactive response, despite being characterised by greater mass and mass moment of inertia of the unsprung masses.

2.3. Preliminary simulations: impact of road irregularities

To analyse the effects of uneven road surfaces on the vertical and longitudinal acceleration oscillations of the sprung mass, the passive configurations (i.e., without any controller intervention being applied to the driver torque demand) of the considered EV architectures – namely, 'In-wheel', '4 on-board', and '2 on-board' – were assessed on a typical uneven road for ride comfort assessment, corresponding to scenario 2 in Section 4.2. The results in Fig. 6 indicate that the ratio between the peaks of the vertical and longitudinal accelerations ranges approximately from 1 to 2, where the highest values are observed for the 'In-wheel' configuration, due to the increased ratio between the unsprung and sprung masses. This highlights the significance of the longitudinal acceleration oscillations, which, although being smaller in magnitude compared to the vertical acceleration oscillations, have a non-negligible impact on the

Fig. 3. The case study demonstrator vehicle at the Lommel proving ground (Belgium).

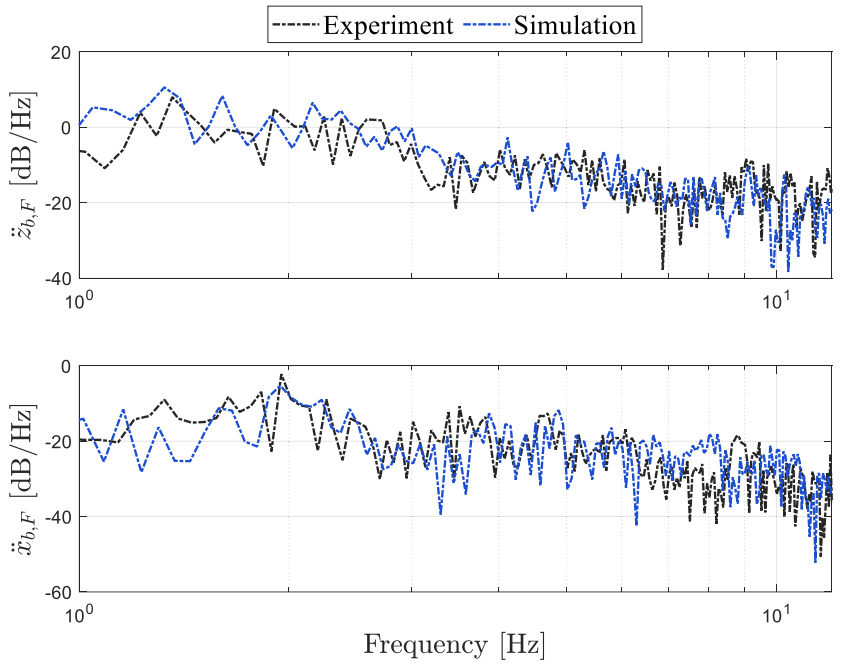

Fig. 4. Experimental validation of the simulation plant along the realistic road profile: PSDs of vertical and longitudinal accelerations of the sprung mass at the front axle.

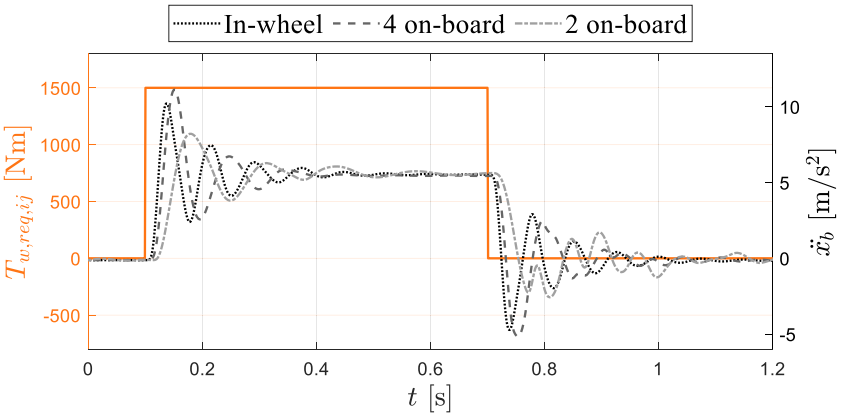

Fig. 5. Profiles of the longitudinal acceleration of the sprung mass for the three nominal parametrisations of the considered powertrain architectures, along a torque tip-in / tip out test, defined by the reference wheel torque profile at the individual corner, $T_{w,req,ij}$.

vehicle ride comfort. The currently available ride comfort enhancement solutions primarily address the compensation of the vertical dynamics of the sprung mass. On the contrary, the study of this paper focuses on the longitudinal vehicle dynamics excited by road irregularities, through the control of on-board powertrains, thus offering potentially broad benefits, since the on-board solutions dominate the electric vehicle market. The outcome is a new control functionality for on-board powertrain architectures, which can complement the more conventional anti-jerk [48] and traction [49] controllers.

3. Nonlinear model predictive control formulation

3.1. Enveloping model

The vertical profile of the road can be obtained through road scanning sensors, which are beyond the scope of this study and already equip production passenger cars with suspension controllers based on road preview, e.g., see the Magic Body Control system by Mercedes-Benz. However, many significant ride events involve excitations generated by irregularities having similar dimension to the tyre contact patch. In such conditions, the road profile measurements from the preview sensor cannot be directly considered as the

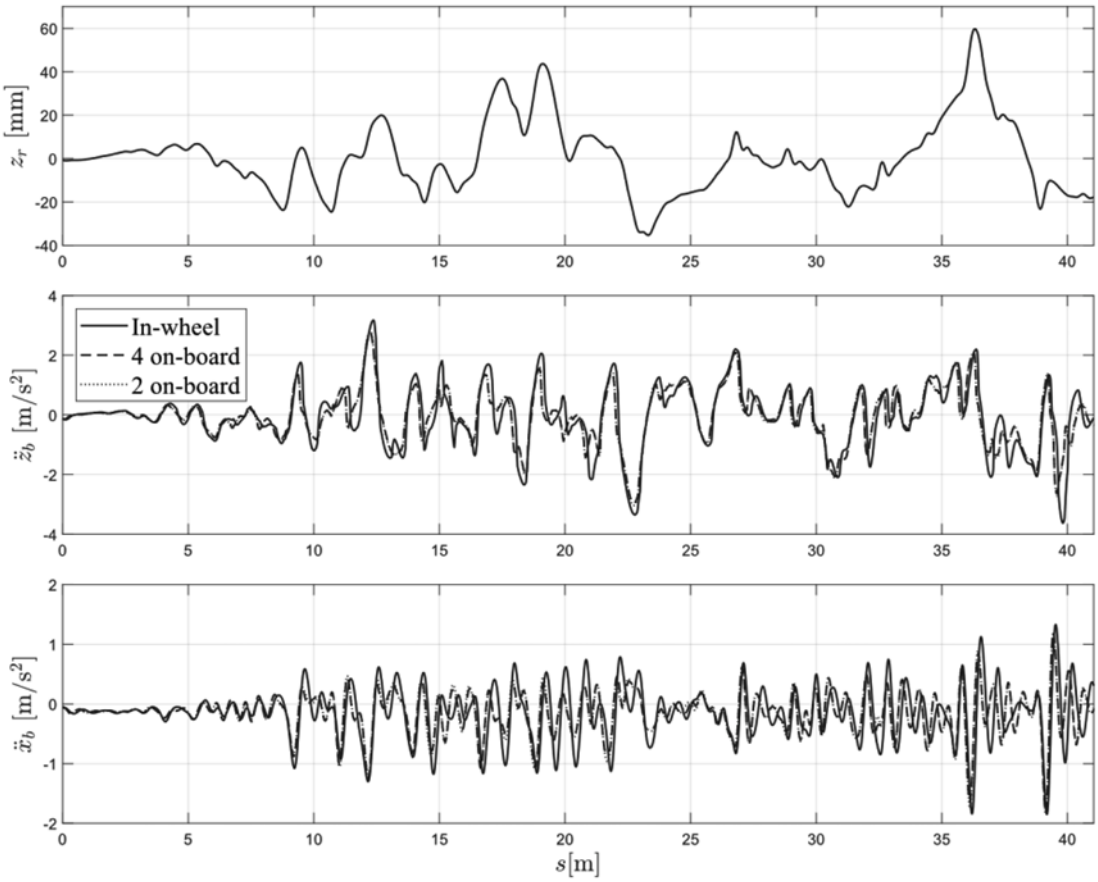

Fig. 6. Road elevation profile (z_r) and the related vertical and longitudinal accelerations of the sprung mass ($\ddot{z}_b$ and $\ddot{x}_b$), for 'In-wheel', '4 on-board', and '2 on-board', on a considered ride comfort road, at a vehicle speed of ~40 km/h.

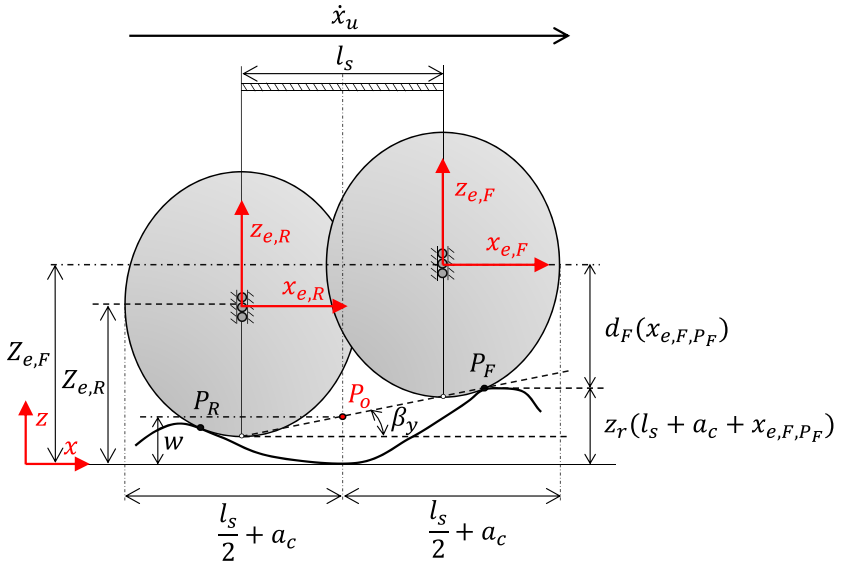

Fig. 7. Schematic of the two-cam tandem configuration of the selected tyre enveloping model, generating the effective road profiles for the NMPCs.

inputs for the simplified dynamic model of the tyre structure, embedded in the NMPCs, especially considering the need – peculiar to the proposed control function – for estimating the longitudinal component of the force excitation associated with the road irregularity. Indeed, a further model describing the geometric filtering behaviour of the tyre contact patch is required. To this purpose, the tandem enveloping model with elliptical cams proposed by Schmeitz in [50] is used to process the raw road profile data, within the online algorithm of the controller. The algorithm was calibrated based on the MF-Swift model embedded in the high-fidelity nonlinear vehicle model for control system assessment, i.e., the plant, and represents a good trade-off between accuracy and computational effort. The enveloping model adopts a geometric formulation that does not imply any numerical integration in the time domain, and outputs the effective road profile variables, namely the effective road height w and slope β_y, provided as external inputs to the NMPCs. The tyre-road contact interface consists of two moving, rigid and identical ellipses, see Fig. 7. Such elliptical cams move longitudinally without rotating, while they independently translate vertically according to the road profile, and maintain a constant relative horizontal distance l_s.

The effective road profile is determined at P_o, which has the same longitudinal coordinate as the wheel centre. w and β_y are functions of the longitudinal wheel position x_u, and depend on the vertical coordinates, $Z_{e,F}$ and $Z_{e,R}$, of the centres of the front and rear cams in the global reference system:

$$w(x_u) = \frac{Z_{e,F} + Z_{e,R}}{2} - b_c$$

$$\tan\beta_y(x_u) = \frac{Z_{e,F} - Z_{e,R}}{l_s} \tag{1}$$

where b_c is the vertical semi-axis of the ellipses. The front ellipse formulation is:

$$\left[\frac{x_{e,F}}{a_c}\right]^c + \left[\frac{z_{e,F}}{b_c}\right]^c = 1 \tag{2}$$

where a_c is the horizontal semi-axis of the ellipse; c is the ellipse shape parameter; and $x_{e,F}$ and $z_{e,F}$ are the axes of the reference system associated with the front ellipse. The bottom profile of the front ellipse, d_F, can be described as a function of $x_{e,F} \in [-a_c,\ a_c]$:

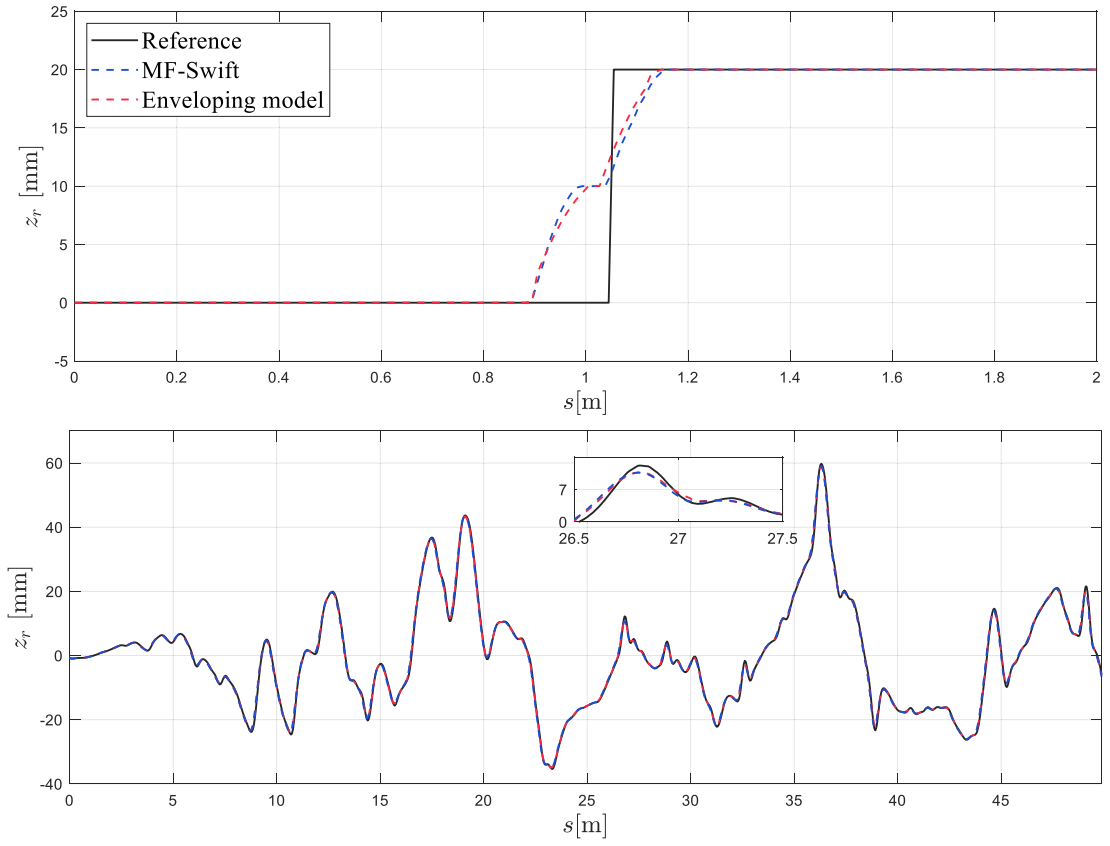

Fig. 8. Comparison of the effective road profiles from the MF-Swift tyre model and the simplified enveloping tandem model, receiving as inputs (Reference) the profiles of: (a) a 20 mm positive step; and (b) an uneven ride comfort assessment road.

$$d_F(x_{e,F}) = b_c\left\{1 - \left[\frac{|x_{e,F}|}{a_c}\right]^c\right\}^{\frac{1}{c}} \tag{3}$$

The corresponding distance for the rear ellipse, d_R, is calculated with the same method. $Z_{e,F}$ and $Z_{e,R}$ are obtained as the highest values of the sum of the road height z_r and the distances d_F and d_R over the feasible range for $x_{e,F}$, with $x_{e,R} \in [\ -a_c,\ a_c]$, for a given longitudinal position of the wheel x_u:

$$Z_{e,F} = \max\left(z_r(x_u, x_{e,F}) + d_F(x_{e,F})\right)$$

$$Z_{e,R} = \max\left(z_r(x_u, x_{e,R}) + d_R(x_{e,R})\right) \tag{4}$$

where z_r depends on the longitudinal position of the wheel and the local longitudinal coordinate in the ellipse reference system.

The two-cam algorithm is calibrated based on the MF-Swift model integrated in the high-fidelity nonlinear vehicle model, which represents the control system assessment plant. The calibration strikes a balance between accuracy and computational efficiency. To assess the reliability of the simplified enveloping model, Fig. 8 displays the road elevation profile from a look-up table (the acquisition method of the road scanning sensor information is outside the scope of this research), indicated as Reference (corresponding to the

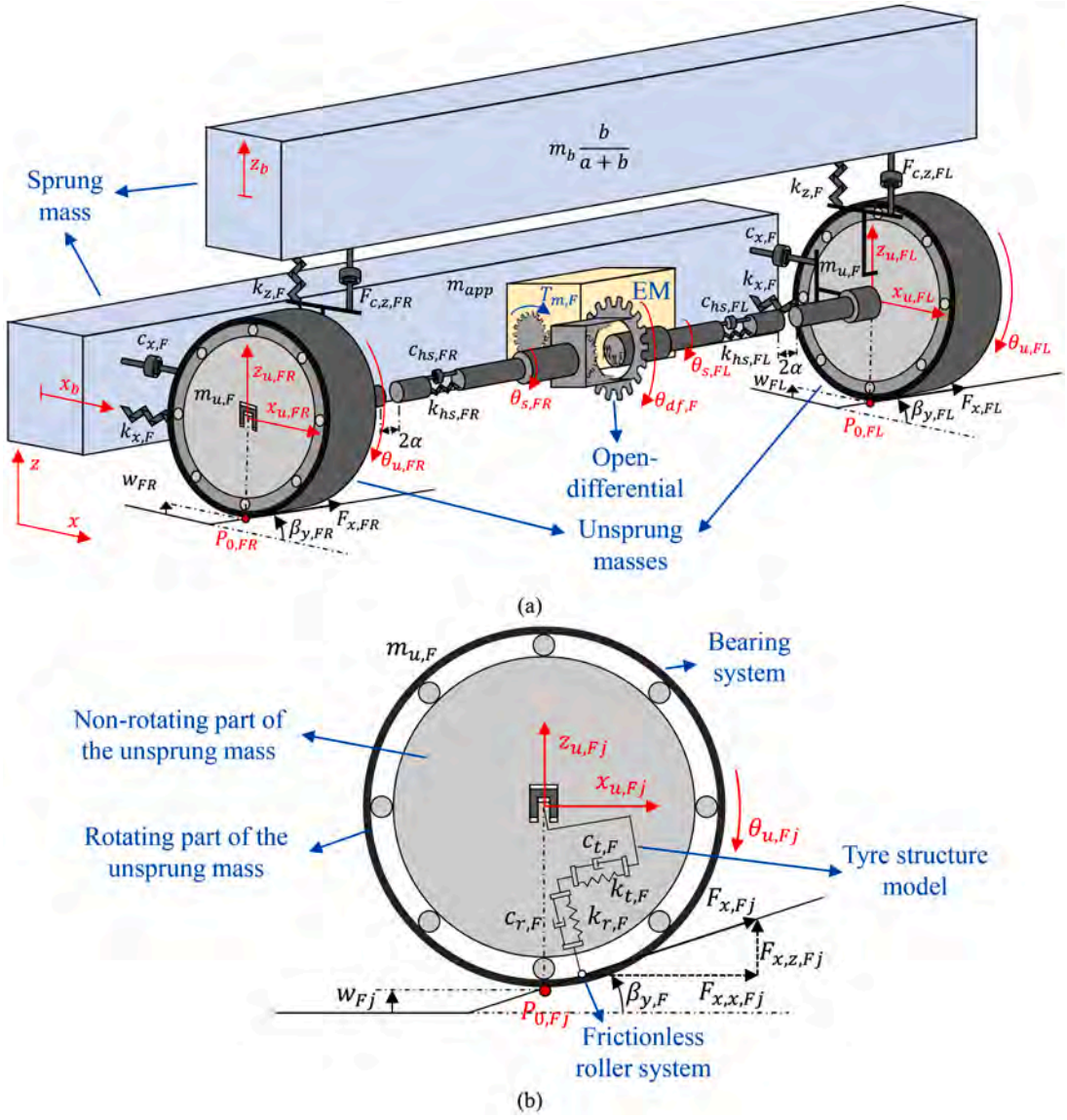

Fig. 9. (a) Three-dimensional schematic of the prediction model of the front axle dynamics of the '2 on-board' configuration; and (b) Side view of an individual unsprung mass model, including the tyre structure model.

road scanning sensor output before the filtering carried out by the selected tyre model formulation), along with the outputs of the MF-Swift model (i.e., the plant) and the two-cam enveloping model (i.e., the formulation within the control structure), in terms of effective road profile for two scenarios: (a) the 20 mm positive step, referred to as scenario 1 in the results; and (b) the uneven ride comfort assessment road, referred to as scenario 2 in the remainder. The excellent match between the two-cam enveloping model and the MF-Swift model confirms the reliability and accuracy of the two-cam enveloping model in absence of road profile variations in the transversal direction of the contact patch.

3.2. Prediction models for '2 on-board'

The prediction models of '2 on-board' are an upgrade of those for in-wheel powertrains in [36], where the enhancement focuses on embedding the torsional drivetrain dynamics typical of the on-board architecture. Each prediction model – see the schematic for the front half of the vehicle in Fig. 9 – of the '2 on-board' case includes: a) the rotational dynamics of the two involved wheels, the longitudinal and vertical dynamics of the two unsprung masses, and the vertical dynamics of the sprung mass, all of them for the relevant front or rear half of the vehicle; b) the longitudinal dynamics of the remaining portion of the whole vehicle, i.e., corresponding to the total sprung mass and the unsprung masses of the other axle w.r.t. the one of the considered prediction model; and c) the axle drivetrain and differential dynamics. Hence, from a mechanical viewpoint, the system is characterized by two degrees of freedom (DoFs) for the sprung mass, six DoFs for the unsprung masses, and two DoFs for the differential dynamics.

For computational efficiency, since the focus of the prediction is to compute the longitudinal dynamics of the unsprung and sprung masses of the considered axle, the model neglects the roll, pitch and yaw dynamics, as well as the longitudinal, vertical and rotational dynamics of the unsprung masses of the other axle. Focusing solely on the dynamics of a single axle or corner within the prediction model markedly decreases the number of states, control inputs, and parameters required for the individual controller, compared to a centralized architecture. This streamlined approach enhances computational efficiency, thereby facilitating the real-time implementation of the resulting implicit NMPCs. Nevertheless, the reference wheel torque values of the other axle are provided to the prediction model of the considered EV half as external inputs, to ensure the realism of the predicted average longitudinal acceleration profile, while the high-frequency disturbances related to the road irregularities are considered only for the two corners of the involved axle. The torsional drivetrain dynamics are included, through the consideration of: i) the electro-magnetic torque dynamics of the EM via a first-order transfer function; ii) a formulation of the open differential behaviour; and iii) appropriate mass moments of inertia linked by torsionally compliant elements [37], including stiffness, damping, and equivalent mechanical backlash. Thus, the system model also considers the typical drivetrain shocks associated with abrupt changes in the delivered torque.

The dynamics of the tyre structure are modelled through two couples of spring-damper systems, the first one radial, with stiffness $k_{r,F}$ and damping coefficient $c_{r,F}$, and the second one tangential, with stiffness $k_{t,F}$ and damping coefficient $c_{t,F}$. The elements of the tyre structure, which transmit their forces directly to the non-rotating part of the unsprung mass, are supposed to be in contact with the road through a frictionless roller system. The longitudinal tyre force caused by the longitudinal tyre slip is independently applied to the rotating part of the unsprung mass, and then to its non-rotating part through a bearing system, see Fig. 9(b). This set-up not only provides acceptable accuracy but also significantly simplifies the formulations in comparison with the MF-Swift tyre model embedded in the high-fidelity vehicle model for control system assessment.

The following equations describe the prediction model dynamics for the front half of the vehicle.

- Vertical force balance of the front sprung mass:

$$\ddot{z}_{b,F} = \left[-F_{k,z,FL} - F_{c,z,FL} - F_{k,z,FR} - F_{c,z,FR} + F_{z,b,F} \right] \frac{1}{m_b} \frac{a+b}{b} \tag{5}$$

where $\ddot{z}_{b,F}$ is the vertical acceleration of the front sprung mass; and $F_{k,z,Fj}$ and $F_{c,z,Fj}$ are the vertical suspension forces of the spring and shock absorber. $F_{k,z,Fj}$ is linearised as:

$$F_{k,z,Fj} = k_{z,F} \left[z_{b,F} - z_{u,Fj} \right] \tag{6}$$

where $k_{z,F}$ is the vertical suspension stiffness; and $z_{b,F}$ and $z_{u,Fj}$ are the vertical displacement of the front sprung and unsprung masses. $F_{c,z,Fj}$ is approximated with a continuous nonlinear function:

$$F_{c,z,Fj} = a_1 + b_1 \operatorname{atan}\left(c_1 \left[\dot{z}_{b,F} - \dot{z}_{u,Fj} \right] + d_1 \right) + b_2 \operatorname{atan}\left(c_2 \left[\dot{z}_{b,F} - \dot{z}_{u,Fj} \right] + d_2 \right) \tag{7}$$

with a_1, b_1, b_2, c_1, c_2, d_1 and d_2 are constant tuneable coefficients. $F_{z,b,F}$ is the equivalent vertical force on the sprung mass associated with the suspension anti-properties (e.g., anti-lift, anti-dive, and anti-squat) contributions, and is calculated as:

$$F_{z,b,F} = F_{z,b,FL} + F_{z,b,FR} = m_{tot} \ddot{x}_b \frac{h_g}{a+b} - F_{z,ap,FL} - F_{z,ap,FR} \tag{8}$$

where $m_{tot} = m_b + 2m_{u,F} + 2m_{u,R}$ is the total vehicle mass; $\ddot{x}_{b,F}$ is the longitudinal acceleration of the sprung mass; and $F_{z,ap,FL}$ and $F_{z,ap,FR}$ are the longitudinal load transfer contributions on the unsprung masses caused by the suspension anti-properties, which are calculated as:

$$F_{z,ap,Fj} = \frac{1}{2} p_T m_{tot} \ddot{x}_b \tan\phi_{Fj} \tag{9}$$

where p_T is the front-to-total distribution ratio of the wheel torque; ϕ_{Fj} is the angle associated with the suspension arm, which is related to the suspension anti-property (-dive, -squat, etc..) coefficient.

- Vertical force balance of each front unsprung mass:

$$\ddot{z}_{u,Fj} = \left[F_{c,z,Fj} + F_{k,z,Fj} + F_{r,z,Fj} - F_{t,z,Fj} + F_{x,z,Fj} + F_{z,ap,Fj}\right] \frac{1}{m_{u,F}} \tag{10}$$

where $m_{u,F}$ is the unsprung mass of the considered front corner; $F_{x,z,Fj}$ (see also Fig. 9(b)) is the vertical component of the traction/braking tyre force $F_{x,Fj}$, computed through version 5.2 of the Magic Formula [51] for zero slip angle conditions in this proof-of-concept implementation; $F_{r,z,Fj}$ and $F_{t,z,Fj}$ are the vertical components of the radial and tangential forces, $F_{r,Fj}$ and $F_{t,Fj}$, related to the tyre structure behaviour. By neglecting the time derivative of $\beta_{y,Fj}$, $F_{r,z,Fj}$ and $F_{t,z,Fj}$ are calculated as:

$$\begin{aligned} F_{r,z,Fj} &= F_{r,Fj}\cos\beta_{y,Fj} = k_{r,F}\left[w_{Fj} - z_{u,Fj}\right]\cos\beta_{y,Fj} + c_{r,F}\left[\dot{w}_{Fj} - \dot{z}_{u,Fj}\right]\cos\beta_{y,Fj} \\ F_{t,z,Fj} &= F_{t,Fj}\sin\beta_{y,Fj} = k_{t,F}\left[w_{Fj} - z_{u,Fj}\right]\sin\beta_{y,Fj} + c_{t,F}\left[\dot{w}_{Fj} - \dot{z}_{u,Fj}\right]\sin\beta_{y,Fj} \end{aligned} \tag{11}$$

where $k_{r,F}$ and $k_{t,F}$ are the radial and tangential stiffness of the tyre; and $c_{r,F}$ and $c_{t,F}$ are the respective damping coefficients.

- Longitudinal force balance of the sprung mass of the whole EV, computed from the viewpoint of the front prediction model, hence the notation $\ddot{x}_{b,F}$ for the acceleration:

$$\ddot{x}_{b,F} = \left[-F_{k,x,FL} - F_{c,x,FL} - F_{k,x,FR} - F_{c,x,FR} + \sum_{j=L,R} \frac{T_{hs,req,Rj}}{R_{lad,Rj}} - F_{drag} - F_{roll,R} \right] \frac{1}{m_{app,F}} \tag{12}$$

where $R_{lad,Rj}$ is the rear laden wheel radius; and $T_{hs,req,Rj}$ is the requested half-shaft torque at the j rear wheel, i.e., $T_{hs,req,Rj} = T_{m,req,R}\,\eta_t i_t/2$, with $i_{t,R}$ being the rear transmission ratio. $F_{k,x,Fj}$ and $F_{c,x,Fj}$ are the stiffness and damping force contributions of the front suspension bushings, which transmit the longitudinal forces to the sprung mass:

$$\begin{aligned} F_{k,x,Fj} &= k_{x,F}\left[x_{b,F} - x_{u,Fj}\right] \\ F_{c,x,Fj} &= c_{x,F}\left[\dot{x}_{b,F} - \dot{x}_{u,Fj}\right] \end{aligned} \tag{13}$$

F_{drag} is the aerodynamic drag force:

$$F_{drag} = \frac{1}{2}\rho_{air} C_d A_{car} \dot{x}_{b,F}^2 \tag{14}$$

where ρ_{air} is the air density; C_d is the aerodynamic drag coefficient; and A_{car} is the frontal vehicle area. $F_{roll,R}$ is the rear rolling resistance force:

$$F_{roll,R} = f_{roll} m_{tot} \frac{a}{a+b} g, \text{ with } f_{roll} = f_{roll,0} + f_{roll,2}\dot{x}_{b,F}^2 \tag{15}$$

where f_{roll} is the rolling resistance coefficient, given by the sum of a constant term ($f_{roll,0}$) and a contribution ($f_{roll,2}\dot{x}_{b,F}^2$) that is a function of speed, and g is the gravitational acceleration. In (12), the apparent mass $m_{app,F}$ is the equivalent mass that includes the effect of the translating and rotating parts of the vehicle that are not modelled in detail within the individual prediction model, i.e., the other wheels. Hence, $m_{app,F}$ accounts for the unsprung masses as well as the mass moments of inertia ($J_{u,y,R}$) of the rotating parts of the rear corners;

$$m_{app,F} = m_b + 2m_{u,R} + 2\frac{J_{u,y,R}}{R_R^2} \tag{16}$$

where R_R is the rolling radius of the rear wheels.

- Longitudinal force balance of each front unsprung mass:

$$\ddot{x}_{u,Fj} = \left[F_{c,x,Fj} + F_{k,x,Fj} - F_{r,x,Fj} - F_{t,x,Fj} + F_{x,x,Fj}\right] \frac{1}{m_{u,F}} \tag{17}$$

where $F_{r,x,Fj}$, $F_{t,x,Fj}$, and $F_{x,x,Fj}$ are the longitudinal components of $F_{r,Fj}$, $F_{t,Fj}$, and $F_{x,Fj}$.

- Moment balance of each front wheel:

$$\ddot{\theta}_{u,Fj} = \left[T_{hs,Fj} - F_{x,Fj} R_{lad,Fj} - M_{roll,Fj}\right] \frac{1}{J_{u,y,F}} \tag{18}$$

where $\ddot{\theta}_{u,Fj}$ is the angular wheel acceleration; and $M_{roll,Fj}$ is the rolling resistance moment. The half-shaft torque $T_{hs,Fj}$ is modelled through stiffness and damping contributions, $T_{hs,k,Fj}$ and $T_{hs,c,Fj}$:

$$T_{hs,Fj} = T_{hs,k,Fj} + T_{hs,c,Fj} \tag{19}$$

To account for the effect of the equivalent angular drivetrain backlash, the spring and damper torque expressions are approximated as:

$$\begin{aligned} T_{hs,k,Fj} &= f_{a,Fj} f_{1,Fj} + f_{b,Fj} f_{2,Fj} \\ T_{hs,c,Fj} &= f_{c,Fj} f_{1,Fj} + f_{c,Fj} f_{2,Fj} \end{aligned} \tag{20}$$

where $f_{a,Fj}$, $f_{b,Fj}$ and $f_{c,Fj}$ are linear functions:

$$\begin{aligned} f_{a,Fj} &= k_{hs,Fj}\left[\theta_{s,Fj} - \theta_{u,Fj} + \alpha\right] \\ f_{b,Fj} &= k_{hs,Fj}\left[\theta_{s,Fj} - \theta_{u,Fj} - \alpha\right] \\ f_{c,Fj} &= c_{hs,Fj}\left[\dot{\theta}_{s,Fj} - \dot{\theta}_{u,Fj}\right] \end{aligned} \tag{21}$$

where $k_{hs,Fj}$ and $c_{hs,Fj}$ are the half-shaft stiffness and damping coefficient; α is half of the equivalent angular backlash; and $\theta_{s,Fj}$ and $\theta_{u,Fj}$ are the angular displacement of the half-shafts and wheels. Moreover, $f_{1,Fj}$ and $f_{2,Fj}$ are switching functions described through exponential formulations:

$$\begin{aligned} f_{1,Fj} &= \frac{1}{2}\left[\frac{1 - f_{1,exp,Fj}}{1 + f_{1,exp,Fj}}\right] + \frac{1}{2} \\ f_{2,Fj} &= \frac{1}{2}\left[\frac{1 - f_{2,exp,Fj}}{1 + f_{2,exp,Fj}}\right] + \frac{1}{2} \end{aligned}$$

with:

$$\begin{aligned} f_{1,exp,Fj} &= \exp\left(2a_d\left\{\alpha - \left[\theta_{s,Fj} - \theta_{u,Fj}\right]\right\}\right) \\ f_{2,exp,Fj} &= \exp\left(2a_d\left\{\alpha + \left[\theta_{s,Fj} - \theta_{u,Fj}\right]\right\}\right) \end{aligned} \tag{22}$$

where a_d is the shape factor of the function, i.e., the higher is a_d, the sharper is the shape of the function. a_d is selected according to a trade-off between an accurate approximation of a linear piecewise function, which would require a high value of a_d, and the requirement of preventing the system from becoming numerically stiff, and generating numerical errors in the solution of the nonlinear optimal control problem, which would need a low value of a_d. The nominal value of the equivalent angular backlash, α, see Table 1, is taken from the literature [52]. The angular displacement $\theta_{s,Fj}$ of the sun gears of the mechanical differential is computed through the Willis equations:

$$\begin{aligned} \dot{\theta}_{s,FL} &= \dot{\theta}_{df,F} - \frac{1}{2}\Delta\dot{\theta}_{s,F} \\ \dot{\theta}_{s,FR} &= \dot{\theta}_{df,F} + \frac{1}{2}\Delta\dot{\theta}_{s,F} \end{aligned} \tag{23}$$

where $\dot{\theta}_{df,F}$ is the angular speed of the differential case; and $\Delta\dot{\theta}_{s,F}$ is the angular speed difference between the sun gears.

- Moment balance equations of the front drivetrain with open differential [40,53]:

$$\ddot{\theta}_{df,F} = \left[4J_{eq,2,F} i_t n_t T_{m,F} - \sum_{j=L,R} 4J_{eq,2,F} T_{hs,Fj} + \Delta J_{hs,F} T_{hs,FR} - \Delta J_{hs,F} T_{hs,FL} \right] \frac{2}{8J_{eq,1,F}\, J_{eq,2,F} - \Delta J_{hs,F}^2} \tag{24}$$

$$\Delta\ddot{\theta}_{s,F} = \left[-2J_{eq,1,F} T_{hs,FR} + 2J_{eq,1,F} T_{hs,FL} - \Delta J_{hs,F} i_t n_t T_{m,F} + \sum_{j=L,R} \Delta J_{hs,F} T_{hs,Fj} \right] \frac{4}{8J_{eq,1,F} J_{eq,2,F} - \Delta J_{hs,F}^2} \tag{25}$$

where $\Delta J_{hs,F}$ is the difference between the mass moments of inertia of the front right and front left half-shafts; $i_{t,F}$ is the front transmission ratio; and $n_{t,F}$ is the front transmission efficiency. The equivalent mass moments of inertia of the front drivetrain, $J_{eq,1,F}$ and $J_{eq,2,F}$, are calculated as:

$$J_{eq,1,F} = J_{mgd,F} + 2J_{s,F} + \frac{\sum_{j=L,R} J_{hs,Fj}}{2}$$

$$J_{eq,2,F} = J_{s,F} + \frac{\sum_{j=L,R} J_{hs,Fj}}{4} + i_p^2 J_{p,F} \tag{26}$$

where $J_{hs,FR}$ and $J_{hs,FL}$ are the moments of inertia of the front right and front left half-shafts; $J_{s,F}$ and $J_{p,F}$ are the moments of inertia of the sun gears and planetary gears of the front differential; i_p is the transmission ratio between sun gear and planetary gear; and $J_{mgd,F}$ is the equivalent moment of inertia of the rotating parts of the front motor, gearbox and differential case.

- Electro-magnetic torque dynamics of the EM:

$$\dot{T}_{m,F} = \left[T_{m,corr,F} - T_{m,F} \right] \frac{1}{\tau_{m,F}} \tag{27}$$

where $T_{m,F}$ is the actual electro-magnetic motor torque; and $\tau_{m,F}$ is the time constant of the EM.

In this and the following prediction model formulations, the longitudinal relaxation dynamics of the tyres are neglected, to reduce the computational effort without significantly compromising performance.

3.3. Prediction model for '4 on-board'

The prediction models of '4 on-board' are similar to those of '2 on-board', with the following differences: a) the individual prediction model considers the dynamics of only one corner, rather than those of the two corners of the same axle; and b) the absence of the mechanical differential dynamics. As a consequence, the system is characterised by two DoFs for the sprung mass, three DoFs for the unsprung mass of the considered corner, and one DoF for the drivetrain dynamics. Given the reduced number of meshing gears and coupling elements compared to '2 on-board', a smaller nominal value of the equivalent backlash is considered, see Table 1. For conciseness, only the equations that significantly change w.r.t. the '2 on-board' case are explicitly reported for the front left corner.

- Vertical force balance of the sprung mass:

$$\ddot{z}_{b,FL} = \left[-F_{k,z,FL} - F_{c,z,FL} \right] \frac{2}{m_b} \frac{a+b}{b} \tag{28}$$

which considers the contributions of the single corner.

- Longitudinal force balance of the sprung mass:

$$\ddot{x}_{b,FL} = \left[-F_{k,x,FL} - F_{c,x,FL} + \frac{T_{hs,req,FR}}{R_{lad,\ FR}} + \frac{T_{hs,req,RL}}{R_{lad,RL}} + \frac{T_{hs,req,RR}}{R_{lad,RR}} - F_{drag} - F_{roll,R} - \frac{F_{roll,F}}{2} \right] \frac{1}{m_{app,FL}} \tag{29}$$

in which m_{app} accounts for the other three corners:

$$m_{app,FL} = m_b + 2m_{u,R} + m_{u,F} + 2\frac{J_{u,y,R}}{R_R^2} + \frac{J_{u,y,F}}{R_F^2} \tag{30}$$

and $F_{roll,F}$ is the rolling resistance force of the front axle:

$$F_{roll,F} = f_{roll} m_{tot} \frac{b}{a+b} g \tag{31}$$

- Moment balance of the drivetrain:

$$\ddot{\theta}_{s,FL} = \left[i_{t,F} n_{t,F} T_{m,FL} - T_{hs,FL} \right] \frac{1}{J_{eq,FL}} \tag{32}$$

where $\ddot{\theta}_{s,FL}$ is the angular acceleration of the front left transmission output shaft; $J_{eq,FL}$ is the equivalent mass moment of inertia of the drivetrain, including the contributions from the EM rotor and transmission shafts; and $T_{m,FL}$ is the actual electro-magnetic motor torque. The wheel moment balance and EM torque dynamics formulations are the same as for '2 on-board'.

3.4. Prediction model for 'In-wheel'

The prediction model of the 'In-wheel' case is the same as for '4 on-board', with the exception of the torsional drivetrain dynamics, which are absent, since the EM rotor can be considered rigidly connected to the wheel. Hence, (18) is modified by replacing the half-shaft torque T_{hs} directly with the actual electromagnetic motor torque T_m:

$$\ddot{\theta}_{u,Fj} = \left[T_{m,Fj} - F_{x,Fj} R_{lad,Fj} - M_{roll,Fj} \right] \frac{1}{J_{u,y,F}} \tag{33}$$

The detailed description of the formulation is reported in [36].

3.5. Nonlinear optimal control problem

At each time step j_c, the NMPC algorithm computes an optimal control input sequence U that minimizes a cost function J, accounting for the prediction of the system dynamics over a predefined horizon t_h, while considering system constraints. The discrete form of the optimal control problem (OCP) formulation is:

$$\underset{U}{\text{argmin}}\ J := J_{terminal} + J_{stage} = \frac{1}{2} \| z_{N_h} - z_{ref,N_h} \|^2_{Q_t} + \frac{1}{2} \sum_{k=j_c}^{j_c+N_h-1} \left[\| z_k - z_{ref,k} \|^2_Q + \| u_k \|^2_R \right]$$

s.t.

$$x_0 = x_{in}$$

$$x_{k+1} = f_d(x_k, u_k, p_k)$$

$$z_k = g_d(x_k, u_k, p_k)$$

$$u_{min} \le u_k \le u_{max} \tag{34}$$

where J consists of a terminal cost, $J_{terminal}$, which aims to minimise the response error at the end of t_h, and a stage cost contribution, J_{stage}, which aims to optimise the response along t_h; k indicates a step along the prediction horizon t_h; N_h is the number of steps of t_h, i.e., $t_h = N_h\ t_s$, with t_s being the sampling time used for discretising the OCP; z is the vector of the predicted system outputs, whose corresponding reference vector is z_{ref}; Q, Q_t and R are positive diagonal weighting matrices; x is the state vector; u is the control input vector; $U = \left[u_{j_c}\ u_{j_c+1} \dots\ u_{j_c+N_h-1} \right]^T$ is the decision variable vector; p is the parameter or external disturbance vector; x_{in} is the initial value of the state vector; f_d is the vector field describing the discretised version of the prediction models in Sections 3.2-3.4, which are arranged in a nonlinear state-space form; g_d is the function expressing the system outputs; and u_{min} and u_{max} are the bounds on the control action u.

In the specific implementations, z consists of $\ddot{x}_b$, which is the main variable related to the longitudinal vehicle comfort level:

$$z_k = \left[\ddot{x}_{b,k} \right] \tag{35}$$

while its reference value z_{ref} is:

$$z_{ref,k} = \left[\ddot{x}_{b,ref,j_c} \right] \tag{36}$$

where $\ddot{x}_{b,ref,k}$ is the target value of the longitudinal acceleration of the vehicle body at each time step, calculated from the longitudinal force balance at the vehicle level:

$$\ddot{x}_{b,ref} = \left[\sum_{i=F,Rj=R,L} \sum \frac{T_{w,req,ij}}{R_{lad,ij}} - F_{roll} - F_{drag} \right] \frac{1}{m_{tot} + 2\frac{J_{u,y,R}}{R_R^2} + 2\frac{J_{u,y,F}}{R_F^2}} \tag{37}$$

where $T_{w,req,ij}$ is the reference wheel torque ($T_{w,req,ij} = T_{hs,req,ij}$ for the on-board cases). The effect of road irregularities on the reference longitudinal acceleration profile is purposely neglected, i.e., the resulting acceleration is the longitudinal acceleration the vehicle would have in absence of road irregularities, which, given the scope of the controller, is the required acceleration value. The control action $u(t)$ is the correction of the motor torque, i.e., ΔT_m. The modified reference EM torque, $T_{m,corr,ij}$, is the sum of the driver torque demand contribution at the motor level, and ΔT_m, i.e., $T_{m,corr,ij} = T_{m,req,ij} + \Delta T_m$. The constraints of the control action are expressed as:

$$Lb_{T_m} \leq T_{m,req,ij} + \Delta T_m \leq Ub_{T_m} \tag{38}$$

where Lb_{T_m} and Ub_{T_m} are the lower and upper motor torque limits.

With reference to Fig. 1, the complexity of the prediction model increases from 'In-wheel' to '2 on-board', passing through '4 on-board', which represents an intermediate case, see the formulations in Sections 3.2-3.4. For example, the state vector for the front left 'In-wheel' prediction model is:

$$x_{FL,In-wheel} = \left[\dot{z}_{b,FL}\ z_{b,FL}\ \dot{z}_{u,FL}\ z_{u,FL}\ \dot{x}_{b,FL}\ x_{b,FL}\ \dot{x}_{u,FL}\ x_{u,FL}\ \dot{\theta}_{u,FL}\ T_{m,FL} \right]^T \tag{39}$$

The inclusion of the torsional half-shaft dynamics in the '4 on-board' prediction model requires two additional states compared to 'In-wheel', i.e., the angular velocity and displacement of the differential side gears, $\dot{\theta}_{s,ij}$ and $\theta_{s,ij}$:

$$x_{FL,4\ on-board} = \left[\dot{z}_{b,FL}\ z_{b,FL}\ \dot{z}_{u,FL}\ z_{u,FL}\ \dot{x}_{b,FL}\ x_{b,FL}\ \dot{x}_{u,FL}\ x_{u,FL}\ \dot{\theta}_{u,FL}\ \theta_{u,FL}\ \dot{\theta}_{s,FL}\ \theta_{s,FL}\ T_{m,FL} \right]^T \tag{40}$$

In the '2 on-board' model, 8 additional states are required to account for the dynamics of both wheels on the same axle (the front one is considered here), the angular velocity $\dot{\theta}_{df,F}$ of the open differential case, and the difference $\Delta\dot{\theta}_{s,F}$ between the angular velocities of the left and right differential side gears:

$$x_{F,2\ on-board} = \left[\dot{z}_{b,F}\ z_{b,F}\ \dot{z}_{u,FL}\ z_{u,FL}\ \dot{z}_{u,FR}\ z_{u,FR}\ \dot{x}_{b,F}\ x_{b,F}\ \dot{x}_{u,FL}\ x_{u,FL}\ \dot{x}_{u,FR}\ x_{u,FR}\ \dot{\theta}_{u,FL}\ \theta_{u,FL}\ \dot{\theta}_{u,FR}\ \theta_{u,FR}\ \theta_{s,FL}\ \theta_{s,FR}\ \dot{\theta}_{df,F}\ \Delta\dot{\theta}_{s,F}\ T_{m,F} \right]^T \tag{41}$$

For 'In-wheel' and '4 on-board', the parameter vector includes the same external inputs, i.e., the expected effective road profile for the single tyre associated with the prediction model, the required EM torque at the considered corner, and the uncorrected wheel motor torque demands of the other corners. This results into:

$$p_{FL,In-wheel} = p_{FL,4\ on-board} = \left[w_{FL}\ \beta_{y,FL}\ T_{m,req,FL}\ T_{m,req,FR}\ T_{m,req,RL}\ T_{m,req,RR} \right]^T \tag{42}$$

For '2 on-board', the parameter matrix is rearranged by considering the presence of two wheels on the same axle and controlled by the same EM:

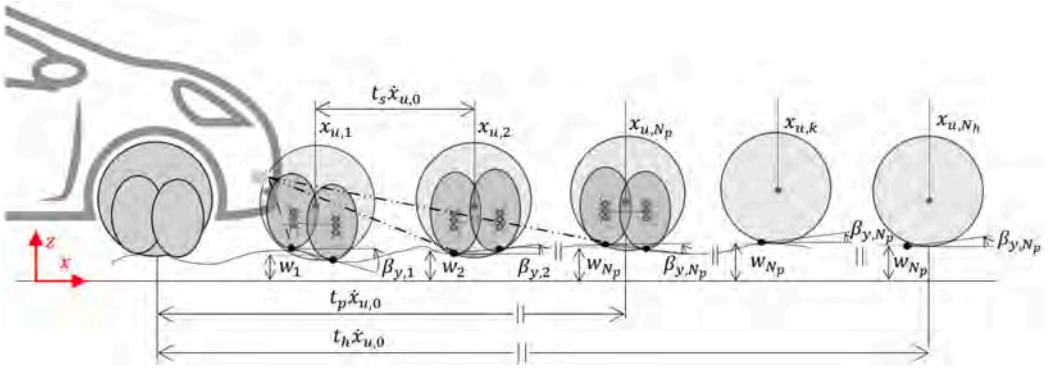

Fig. 10. Schematic of the road preview concept.

$$p_{F,2\ on-board} = \left[w_{FL}\ \beta_{y,FL}\ w_{FR}\ \beta_{y,FR}\ T_{m,req,F}\ T_{m,req,R} \right]^T \tag{43}$$

For the on-board cases, the reference half-shaft torque levels corresponding to the EM torque demands are obtained through the appropriate gear ratios. Future studies will incorporate additional parameters, such as the estimated tyre-road friction factor, and develop further road-preview based control functionalities, including anti-jerk and traction controllers, through modifications of the NMPC cost function.

3.6. Road preview concept

The NMPC prediction model requires the road information from the enveloping model, i.e., the sequence of w and β_y values along the preview time $t_p = N_p t_s$, where N_p is the number of preview steps. A simplified schematic of the road preview concept is shown in Fig. 10.

The preview time is the same or shorter than the prediction horizon t_h. In this application, t_h is considered sufficiently short to assume absence of vehicle speed variation. By making this assumption, the wheel positions along the prediction steps can be obtained as $x_{u,k} = x_{u,0} + \dot{x}_{u,0} t_s k$, where $x_{u,0}$ and $\dot{x}_{u,0}$ represent the initial vehicle position and longitudinal speed. If $t_h > t_p$, the effective road profile is kept constant and equal to the last measured value for the portion of the prediction in which $t > t_p$:

$$W = \left[w_0, w_1, \ldots,\ w_{N_p-1},\ w_{N_p},\ \ldots w_{N_p} \right]$$

$$B_y = \left[\beta_{y,0},\ \beta_{y,1}, \cdots,\ \beta_{y,N_p-1},\ \beta_{y,N_p},\ \cdots,\ \beta_{y,N_p} \right] \tag{44}$$

4. Controller implementation and assessment

4.1. Controller implementation

The nonlinear optimal control problem of the NMPC formulations in Section 3 was solved online – through an implicit approach – by using the ACADO Toolkit, i.e., an open-source tool focused on nonlinear and multi-objective optimal control problems. The discretized nonlinear optimal control problem is converted into a Quadratic Programming (QP) problem, which is solved by the qpOASES 3 solver. The Matlab interface allows to directly export, compile, and use autogenerated C code for NMPCs, also enabling real-time implementation [54]. Unless otherwise specified, in the remainder the controller sampling time, t_s, i.e., the time step at which the algorithm generates the sequence of control inputs, is set to 1 ms, which is equal to the discretization time, t_d, used for the integration of the prediction model along the prediction horizon; and the number of iterations, N_{iter}, carried out by the solver for the computation of the control solution at each sampling time, is set to 3. Such parametrisations are consistent with the proof-of-concept nature of the study, focused on preliminary simulations to explore the performance potential of the controllers, and with the expected future improvement of the computational capabilities of automotive control hardware. Nevertheless, to highlight currently implementable solutions, the following Section 6 will also discuss the parametrisations of real-time set-ups of the proposed algorithms with available control hardware. In the simulations, the pure time delays associated with signal transmission and processing are neglected, since the relevant sensors are going to be hard wired on the control unit, given the highly dynamic nature of the involved phenomena. In the results, the versions of the controllers embedding road preview are referred to as NMPC$^{(prev)}$, while those excluding preview are indicated as NMPC$^{(w/o\ prev)}$.

4.2. Considered road profiles

The performance assessment of the proposed NMPCs has been carried out for the following scenarios:

- Scenario 1, corresponding to a 20 mm positive step of the road profile, with absence or presence of an offset Δx_r between the longitudinal coordinate of the step applied to the right and left wheels, which implies a symmetric or asymmetric road input.
- Scenarios 2-5, based on sections of uneven ride comfort assessment roads, normally used as references by the industrial partner involved in the project.
- An experimentally implemented scenario, consisting of a speed bump measuring 3 cm in height and 25 cm in width.

4.3. Key performance indicators

The considered key performance indicators (KPIs) are based on the typical objective metrics to assess ride comfort [55], and are:

- $RMS_{\ddot{x}_b}$, i.e., the root mean square error value of the longitudinal acceleration $\ddot{x}_b$ of the vehicle w.r.t. its steady-state reference value, $\ddot{x}_{b,ref}$:

$$RMS_{\ddot{x}_b} = \sqrt{\frac{1}{T_2 - T_1} \int_{T_1}^{T_2} \left[\ddot{x}_b - \ddot{x}_{b,ref} \right]^2 dt} \tag{45}$$

- $VDV_{\ddot{x}_b}$, i.e., the fourth power longitudinal acceleration vibration dose value, which accounts for the impulsive nature of the involved phenomena, and thus tends to amplify the significance of the peak values of $\ddot{x}_b - \ddot{x}_{b,ref}$, w.r.t. $RMS_{\ddot{x}_b}$:

$$VDV_{\ddot{x}_b} = \sqrt[4]{\int_{T_1}^{T_2} \left[\ddot{x}_b - \ddot{x}_{b,ref} \right]^4 dt} \tag{46}$$

- $RMS_{\dddot{x}_b}$, i.e., the root mean square value of the longitudinal jerk of the vehicle, $\dddot{x}_b$, i.e., the time derivative of the longitudinal acceleration:

$$RMS_{\dddot{x}_b} = \sqrt{\frac{1}{T_2 - T_1} \int_{T_1}^{T_2} \dddot{x}_b^{\,2} dt} \tag{47}$$

- $\Delta\ddot{x}_{b,max}$, i.e., the maximum longitudinal acceleration error:

$$\Delta\ddot{x}_{b,max} = \max\left(\left| \ddot{x}_b - \ddot{x}_{b,ref} \right| \right) \tag{48}$$

where T_1 and T_2, for all KPIs, are the initial and final times of the relevant part of the test.

4.4. Weight optimisation routine

In the simulation analyses of Section 5, a brute force optimisation routine is repeatedly used for the computation of the cost function weights Q, Q_t and R in (34). The routine is based on iteratively and automatically running the simulation and control environment in Fig. 1, by independently varying the individual values of the components of Q, Q_t and R, within a reasonable a priori defined and appropriately discretised parameter space. The weights are selected to minimise the weight tuning cost function J_{WT}, according to:

$$\begin{aligned} &\underset{Q,Q_t,R}{\text{argmin}}\ J_{WT} := w_{1,WT}\ RMS_{\ddot{x}_b} + w_{2,WT}\ VDV_{\ddot{x}_b} \\ &s.t. \\ &Q,\ Q_t \in [Q_{min}, Q_{max}] \\ &R \in [R_{min}, R_{max}] \end{aligned} \tag{49}$$

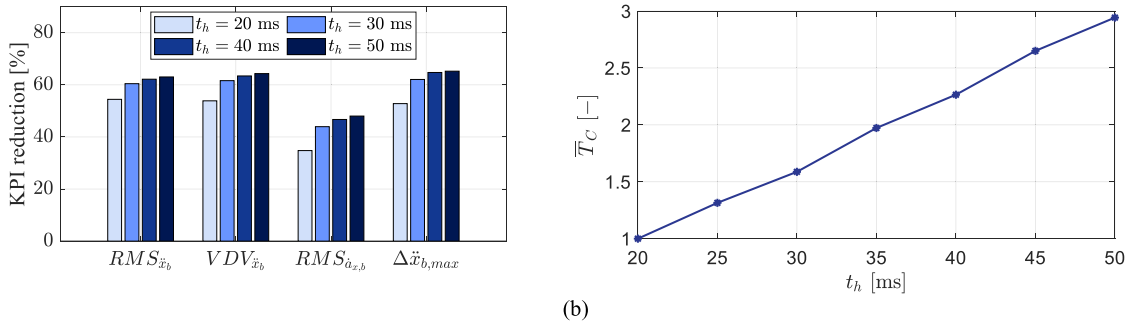

(a) (b)

Fig. 11. Sensitivity analysis of the effect of the prediction horizon t_h on the NMPC$^{(prev)}$ performance for the '4 on-board' configuration, during a symmetric road step test at zero torque demand, from 40 km/h. (a) KPI percentage reduction w.r.t. the passive vehicle, for different t_h values; and (b) nondimensional computational time, $\overline{T}_c$, as a function of t_h.

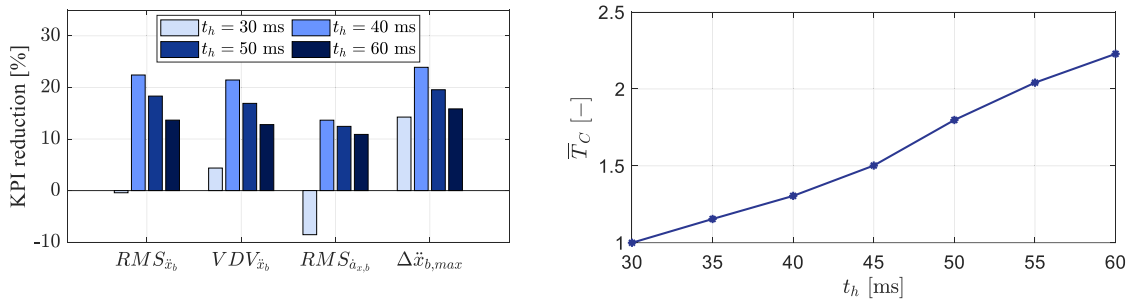

Fig. 12. Sensitivity analysis of the effect of t_h on the NMPC$^{(prev)}$ performance for the '2 on-board' configuration, during a symmetric road step test at zero torque demand, from 40 km/h. (a) KPI percentage reduction w.r.t. the passive vehicle, for different t_h values; and (b) $\overline{T}_c$ as a function of t_h.

where $w_{1,WT}$ and $w_{2,WT}$ are the J_{WT} weights associated with $RMS_{\ddot{x}_b}$ and $VDV_{\ddot{x}_b}$, while Q_{min}, Q_{max}, R_{min}, and R_{max} are the matrices containing the boundaries of the NMPC cost function weights.

5. Simulation results

5.1. Sensitivity analysis on prediction horizon

The target is to identify the most suitable prediction horizon t_h for the proposed NMPC$^{(prev)}$ algorithms, applied to the three considered powertrain architectures. The sensitivity w.r.t. t_h is carried out for a localized road input event, i.e., the step of scenario 1 with $\Delta x_r = 0$, at zero total torque demand, $T_{w,req}$, and from an initial longitudinal speed, $\dot{x}_{b,in}$, of 40 km/h. The cost function weight matrices, i.e., Q, Q_t and R, are maintained constant when varying t_h, and are optimized for each drivetrain configuration for $t_h = 30$ ms, through the routine in Section 4.4. For fairness of comparison, the road preview horizon, t_p, is kept constant and equal to 10 ms for all the t_h sensitivity simulations. Both t_h and t_p are discretized at 1 ms.

The effect of t_h is evaluated in terms of: i) percentage reduction of the selected KPIs w.r.t. the passive configuration (subplots (a) of Figs. 11 and 12); and ii) computational effort, expressed by the nondimensional computational time, $\overline{T}_c$, i.e., the average time required to obtain the solution of the nonlinear optimal control problem, which is normalised w.r.t. the average computational time for the lowest considered prediction horizon (subplots (b) of the same figures). The analysis has already been presented for the 'In-wheel' case in [36], while Fig. 11 and Fig. 12 extend it to the dedicated controllers for the '4 on-board' and '2 on-board' configurations. The performance of '4 on-board' progressively improves as the prediction horizon increases. On the contrary, '2 on-board' reaches maximum performance at $t_h = 40$ ms, after which all the KPIs are characterised by a decay. The reason for the performance loss at high prediction horizons was mainly identified in the increase of the cumulative error caused by the mismatch between plant and prediction model, see similar observations for different NMPC applications in [56,57]. Instead, the same approximately linearly increasing trend for the two configurations can be observed in terms of $\overline{T}_c$, see Fig. 11(b) and Fig. 12(b). In summary, $t_h = 30$ ms and $t_h = 40$ ms represent a good trade-off between performance and computational effort for '4 on-board' and '2 on-board', respectively. Hence, these prediction horizon values are used for the following simulations. Moreover, in the remainder, the 'In-wheel' controllers will adopt the same prediction horizon as '4 on-board'.

A similar sensitivity analysis was run for t_p, based on which the preview time is set to $t_p = 25$ ms in the NMPC$^{(prev)}$ implementations for 'In-wheel' and '4 on-board', while for the slower '2 on-board' the selection is $t_p = 30$ ms.

5.2. Controller evaluation along scenario 1 at zero torque demand

The objective is to explore the potential performance of the preview-based NMPCs when their calibrations for each powertrain layout are optimized for the test conditions in Figs. 11-12. In fact, in road preview implementations, it would be possible to identify the road profile typology in advance, and switch the controller tuning, i.e., the set of cost function weights, to be the most appropriate one for the input ahead.

Fig. 13 includes the profiles of the main variables as a function of the travelled distance, for the three powertrain architectures, for the passive vehicle and the vehicle controlled by the NMPCs including and excluding preview. The top subplots show the longitudinal acceleration, $\ddot{x}_b$. The second row of graphs reports the reference EM torque profiles after the correction carried out by the proposed longitudinal controllers, when present. Given the symmetry of the selected road inputs, the response is identical on the left and right vehicle sides. Hence, for 'In-wheel' and '4 on-board', the graphs plot only the left torque profiles, while for '2 on-board' they report the torque of the central motor of each axle. The bottom plots show the effective powertrain torque at the wheel, T_w, for the 'In-wheel' case, including consideration of the electric drive dynamics, and the left half-shaft torque, T_{hs}, for the on-board cases. The related KPIs are in Table 2. The results highlight that the road preview has an evident effect for a localized event such as the considered step, as it allows to significantly reduce the first acceleration peak by requesting a timely motor torque increase, which prevents the vehicle

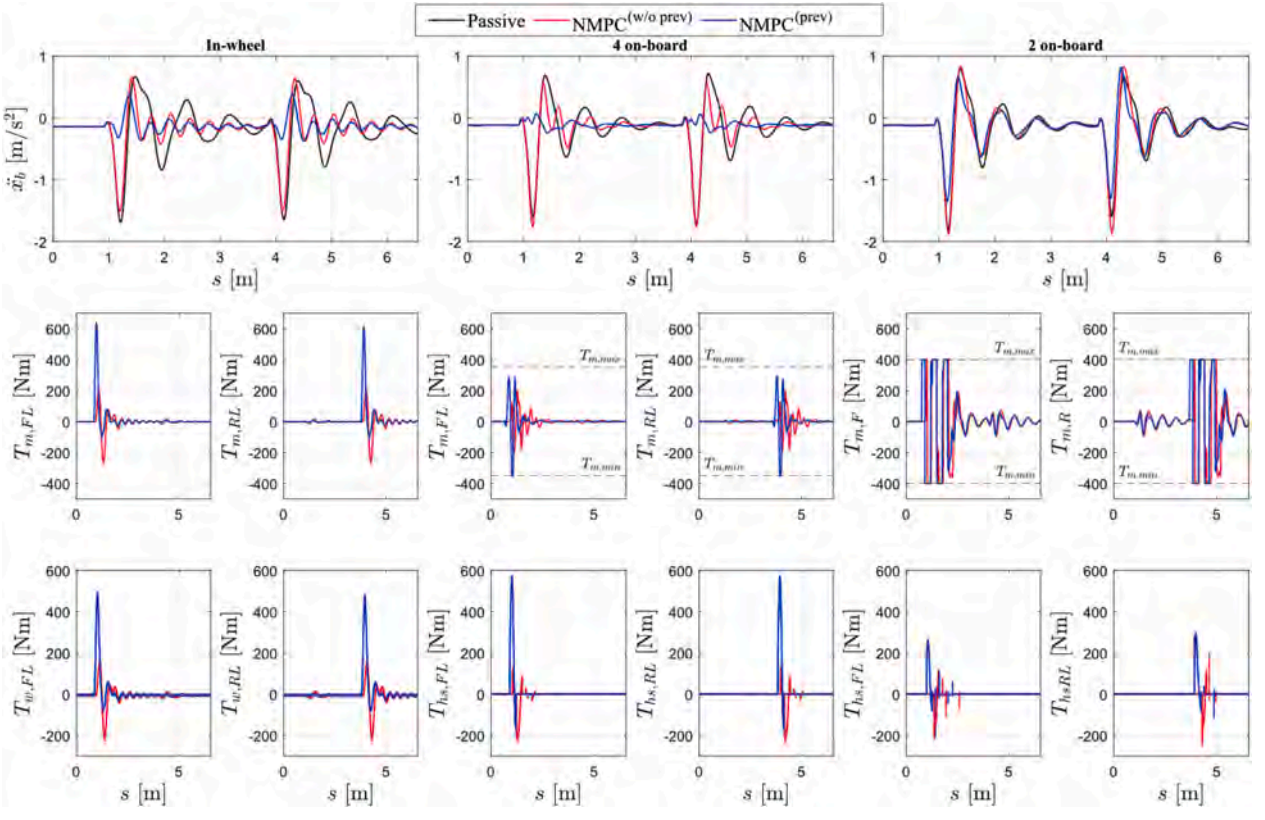

Fig. 13. Performance comparison of the passive, NMPC$^{(w/o\ prev)}$, and NMPC$^{(prev)}$ settings, for 'In-wheel', '4 on-board', and '2 on-board', along the considered symmetric road step test at zero torque demand, from an initial speed of 40 km/h.

Table 2
KPI values for the considered controllers and powertrain configurations. The bold fonts refer to the real-time capable controller settings, see Section 6.1.

$T_{w,req}$ [Nm]	Configuration	In-wheel				4 on-board				2 on-board			
		$RMS_{\ddot{x}_b}$ [m/s^2]	$VDV_{\ddot{x}_b}$ [m/s$^{1.75}$]	$RMS_{\dddot{x}_b}$ [m/s^3]	$\Delta\ddot{x}_{b,max}$ [m/s^2]	$RMS_{\ddot{x}_b}$ [m/s^2]	$VDV_{\ddot{x}_b}$ [m/s$^{1.75}$]	$RMS_{\dddot{x}_b}$ [m/s^3]	$\Delta\ddot{x}_{b,max}$ [m/s^2]	$RMS_{\ddot{x}_b}$ [m/s^2]	$VDV_{\ddot{x}_b}$ [m/s$^{1.75}$]	$RMS_{\dddot{x}_b}$ [m/s^3]	$\Delta\ddot{x}_{b,max}$ [m/s^2]
$\dot{x}_{b,in}$ = 20 km/h													
0	Passive	0.373	0.702	31.3	1.662	0.327	0.595	32.0	1.488	0.324	0.562	31.4	1.377
	NMPC$^{(w/o\ prev)}$	0.217	0.514	19.9	1.310	0.283	0.592	26.6	1.492	0.316	0.634	32.1	1.599
	NMPC$^{(prev)}$	0.059	0.101	9.5	0.241	0.084	0.160	8.7	0.442	0.228	0.403	22.6	0.967
$\dot{x}_{b,in}$ = 40 km/h													
0	Passive	0.419	0.581	44.6	1.547	0.370	0.561	47.0	1.612	0.382	0.574	48.8	1.684
	NMPC$^{(w/o\ prev)}$	0.316	0.504	44.6	1.375	0.331	0.574	49.1	1.650	0.399	0.627	52.6	1.751
	NMPC$^{(prev)}$	0.099	0.135	16.4	0.345	0.045	0.063	8.1	0.178	0.293	0.440	42.6	1.231
1200	Passive	0.385	0.544	42.0	1.467	0.318	0.502	41.9	1.475	0.305	0.495	41.6	1.480
	NMPC$^{(w/o\ prev)}$	0.343	0.535	40.5	1.486	0.297	0.476	46.4	1.420	0.274	0.482	39.6	1.435
	NMPC$^{(prev)}$	0.103	0.147	18.1	0.448	0.131	0.173	19.0	0.507	0.204	0.330	33.5	0.989
2400	Passive	0.335	0.536	37.1	1.545	0.299	0.479	40.1	1.465	0.312	0.469	43.9	1.465
	NMPC$^{(w/o\ prev)}$	0.295	0.513	35.6	1.488	0.273	0.444	43.2	1.376	0.301	0.478	42.9	1.463
	NMPC$^{(prev)}$	0.116	0.161	17.5	0.451	0.173	0.225	25.6	0.709	0.230	0.326	37.4	0.954
$\dot{x}_{b,in}$ = 40 km/h with real-time implementation settings													
0	NMPC$^{(w/o\ prev)}$	**0.344**	**0.540**	**46.5**	**1.453**	**0.343**	**0.597**	**49.5**	**1.698**	**0.421**	**0.631**	**53.8**	**1.751**
	NMPC$^{(prev)}$	**0.142**	**0.173**	**22.9**	**0.421**	**0.124**	**0.201**	**21.9**	**0.602**	**0.369**	**0.533**	**51.7**	**1.371**
$\dot{x}_{b,in}$ = 80 km/h													
0	Passive	0.387	0.436	42.1	1.249	0.385	0.398	55.1	1.058	0.351	0.428	49.7	1.144
	NMPC$^{(w/o\ prev)}$	0.262	0.346	40.1	0.965	0.366	0.424	57.4	1.177	0.365	0.446	51.3	1.202
	NMPC$^{(prev)}$	0.081	0.099	13.6	0.278	0.105	0.097	21.9	0.265	0.326	0.398	47.8	1.043

deceleration caused by the initial impact with the road irregularity. While the preview benefit has already been explored for the 'In-wheel' case, see [36], the new simulations of this section show that the preview controllers can effectively work for the on-board configurations as well, thanks to the inclusion of the torsional drivetrain dynamics and equivalent drivetrain backlash in the prediction model formulations. In fact, the NMPC$^{(prev)}$ set-ups bring a generalized improvement in terms of longitudinal acceleration response, by reducing the associated KPIs by >82% for '4 on-board', and from ~12% to >26% for '2 on-board', see Table 2. On the other hand, NMPC$^{(w/o\ prev)}$ only causes a minor response enhancement for 'In-wheel', and no improvement at all for the on-board cases, due to the purely reactive nature of the algorithm and the inherent response delay caused by the torsional drivetrain dynamics and EM characteristics.

5.3. Effect of initial speed and torque demand

The scenario 1 simulations have been extended to verify the controller performance along a wider range of initial speeds and torque demands, i.e., the test at zero torque demand has been carried out also from 20 and 80 km/h, while the manoeuvre from 40 km/h has been performed for additional wheel torque demands of 1200 and 2400 Nm. In the meantime, the cost function weight matrices of NMPC$^{(prev)}$ have been optimised to vary as a function of speed and torque in the form of maps, for each powertrain configuration. The same look-up tables of the weights are used for NMPC$^{(w/o\ prev)}$.

Similarly to the test of Section 5.2, w.r.t. the passive case, the purely reactive NMPC$^{(w/o\ prev)}$ guarantees a marginal performance improvement for 'In-wheel', while for the on-board layouts NMPC$^{(w/o\ prev)}$ implies a marginal performance decay in some cases, e.g., for zero torque demand and 80 km/h, in which all indicators are worse with the exception of $RMS_{\ddot{x}_b}$, and for $\dot{x}_{b,in} = 40$ km/h and $T_{w,req} = 2400$ Nm, in which for '2 on-board' $VDV_{\ddot{x}_b}$ is higher than for the passive setting, see Table 2. On the contrary, NMPC$^{(prev)}$ enhances the performance for all powertrains. This is especially evident with the 'In-wheel' architecture, e.g., with $RMS_{\ddot{x}_b}$ reductions exceeding 79% and 65% w.r.t. the passive case, respectively for the previous two testing conditions ($\dot{x}_{b,in} = 80$ km/h and $T_{w,req} = 0$ Nm; $\dot{x}_{b,in} = 40$ km/h and $T_{w,req} = 2400$ Nm) that are especially critical for NMPC$^{(w/o\ prev)}$. The '4 on-board' results denote a progressive decrease of the performance improvement brought by NMPC$^{(prev)}$, for increasing values of vehicle speed and torque demand, which are respectively associated with faster drivetrain dynamics and lower magnitude of the initial EM torque increase applicable by the controller, to compensate the effect of the road step. Nevertheless, NMPC$^{(prev)}$ still guarantees a generalized and evident improvement of the '4 on-board' acceleration related indicators, which exceeds 72% at 80 km/h and 42% at $T_{w,req} = 2400$ Nm. At 80 km/h, the slow response of the '2 on-board' motors implies marginal attenuation of the longitudinal acceleration oscillations w.r.t. the passive EV, e.g., amounting to ~7% in terms of $RMS_{\ddot{x}_b}$ and $VDV_{\ddot{x}_b}$, and ~9% in terms of $\Delta\ddot{x}_{b,max}$. It was verified that the adoption of a more performing EM would guarantee a trend in line with the one of the '4 on-board' architecture.

In summary, the important and novel conclusion is that the proposed road preview-based controller formulations can achieve tangible comfort improvements at low-to-medium torque demands for a wide range of vehicle speeds, regardless the powertrain and drivetrain architecture.

5.4. Sensitivity analysis on powertrain and drivetrain parameters for '4 on-board'

The scope of this analysis is to understand the effect of the main powertrain and drivetrain parameters on the potential NMPC$^{(prev)}$ performance with the '4 on-board' configuration, for the test condition in Section 5.1. The sensitivity is carried out w.r.t.: i) the electric drive time constant τ_m; ii) the equivalent inertia J_{eq} of the motor rotor and drivetrain components referred to the wheels; iii) the torsion half-shaft stiffness k_{hs}; and iv) the equivalent drivetrain backlash 2α.

Fig. 14 reports the KPIs as functions of τ_m, J_{eq}, and k_{hs}, for simulations in which the cost function weights have been optimized for the corresponding parameter set. A very wide range of EM time constants, extending beyond the limit of the industrially available solutions, is considered. As τ_m increases, which corresponds to slower EM response, the NMPC$^{(prev)}$ KPIs progressively worsen according to a logarithmic trend, but still guarantee a benefit w.r.t. the passive case, also for $\tau_m > 100$ ms. From 6 to 25 ms, where the latter value corresponds to the time constant of the '2 on-board' case, $RMS_{\ddot{x}_b}$ and $\Delta\ddot{x}_{b,max}$ range from 0.049 to 0.138 m/s^2 and from 0.182 to 0.621 m/s^2 respectively, corresponding to improvements in excess of 60% w.r.t. the passive set-up. As the equivalent inertia J_{eq} increases, the KPIs have an approximately linearly increasing trend. Despite this, also for a very high inertia, i.e., $J_{eq} = 2.8$ kgm^2, NMPC$^{(prev)}$ still improves all the indicators by >60%. For the analysis of the half-shaft stiffness, a range from 5000 to 12500 Nm/rad is considered, which includes the typical values for production cars. The increase in stiffness reduces the half-shaft torsion, and therefore brings quicker wheel torque response, with better overall performance.

Fig. 15 deals with a dedicated sensitivity analysis on the equivalent drivetrain backlash at the wheels, which is carried out for four combinations of system parameters, among those in Fig. 14, namely: i) $\tau_m = 6$ ms, $k_{hs} = 7700$ Nm/rad, and $J_{eq} = 1.4$ kgm^2, referred to as 'Variant A' in the figure; ii) a configuration with increased EM time constant, i.e., with $\tau_m = 25$ ms, $k_{hs} = 7700$ Nm/rad, and $J_{eq} = 1.4$ kgm^2 ('Variant B'); iii) a configuration with the same EM time constant as in ii) and reduced half-shaft stiffness, i.e., with $\tau_m = 25$ ms, $k_{hs} = 6500$ Nm/rad, and $J_{eq} = 1.4$ kgm^2 ('Variant C'); and iv) a configuration also including an increased powertrain inertia, corresponding to $\tau_m = 25$ ms, $k_{hs} = 6500$ Nm/rad, and $J_{eq} = 2.8$ kgm^2 ('Variant D').

The figure reports the percentage reduction of the KPIs w.r.t. the passive case. The controller cost function weights are optimized for each variant in the condition with low equivalent backlash, i.e., $2\alpha = 1.2$ deg, for a total of four control settings. Each variant is then assessed for a wide range of values of 2α, i.e., $2\alpha = 1.2$, 3.5, 6.0, and 10 deg. These can occur during the vehicle lifetime, because of drivetrain component wear. In the sensitivity, the increased backlash value is included both in the plant model and the prediction

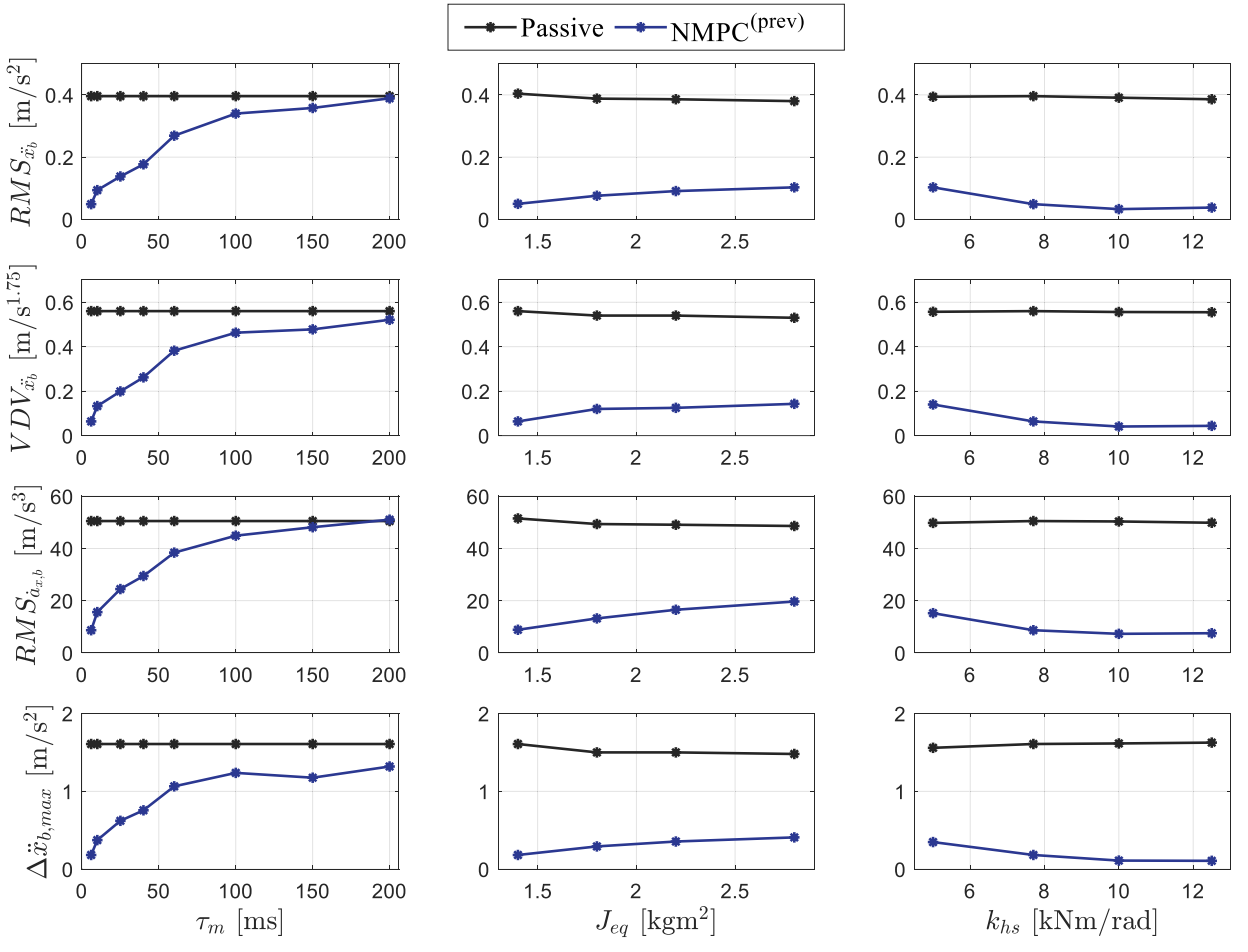

Fig. 14. KPI profiles for NMPC$^{(prev)}$ and the passive EV, as a function of the motor time constant τ_m, the equivalent inertia J_{eq}, and the torsion half-shaft stiffness k_{hs}, for '4 on-board', along the considered symmetric road step test at zero torque demand, from an initial speed of 40 km/h.

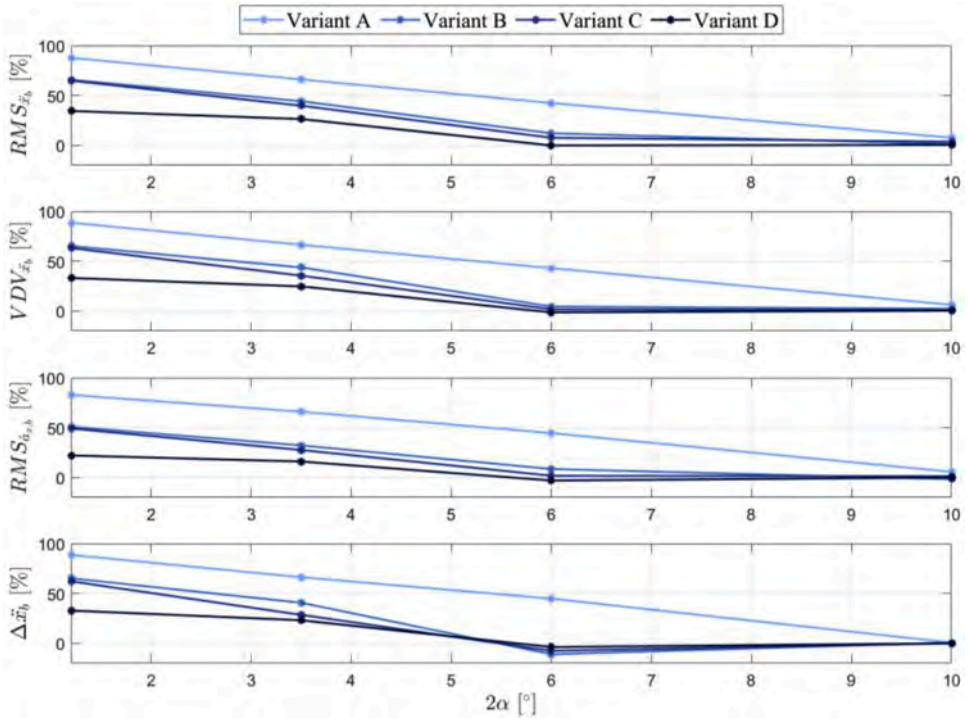

Fig. 15. KPI percentage reduction w.r.t. the passive case as a function of the backlash 2α, for variants A-D of the '4 on-board' configuration.

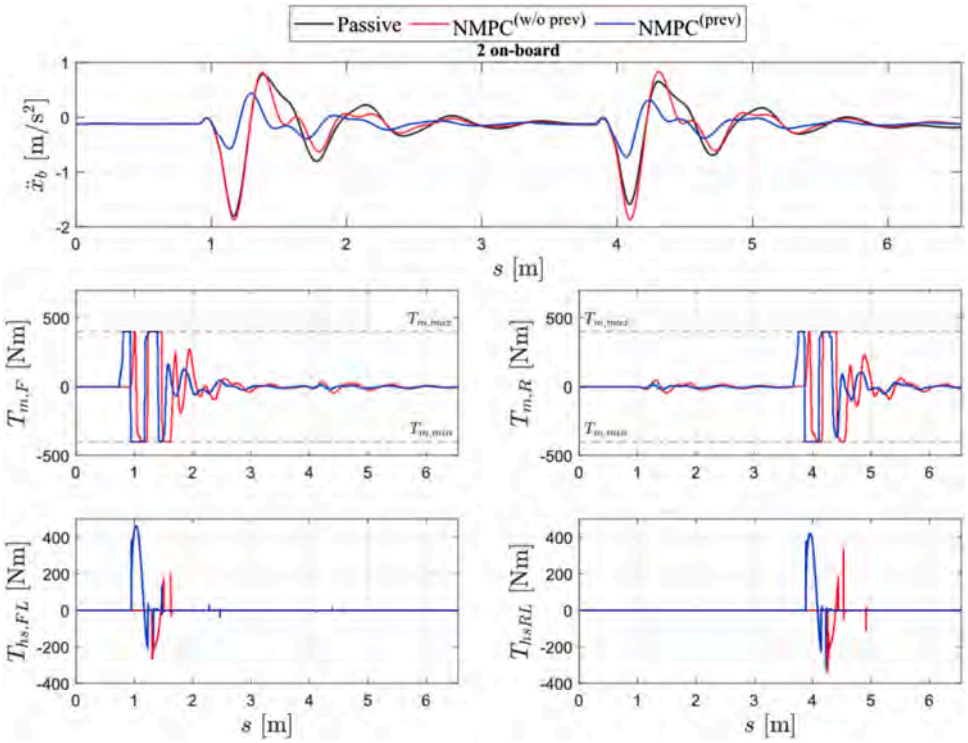

Fig. 16. Performance comparison of the passive, NMPC$^{(\text{w/o prev})}$, and NMPC$^{(\text{prev})}$ configurations, for '2 on-board', along the considered symmetric road step test at zero torque demand, from an initial speed of 40 km/h, and for an EM time constant $\tau_m = 5.7$ ms.

model, since effective drivetrain backlash estimation algorithms are available from the literature [58,59]. On the contrary, the controller cost function weights are kept constant as a function of the backlash magnitude.

The results highlight that: i) although the passive versions behave very similarly in terms of KPIs, with variations that are less than 15% across the parameter range, which is also evident from the results in Fig. 14, the controlled configurations are characterised by significant variability of the KPIs; ii) the proposed preview controller brings tangible benefits up to $2\alpha =$ 6 deg, which corresponds to a meaningful range of drivetrain backlash for practical applications; iii) for a given value of backlash magnitude, apart from an exception for a single indicator ($\Delta\ddot{x}_{b,max}$) for $2\alpha = 6$ deg, variants A to D order themselves according to the performance enhancement brought by NMPC$^{(prev)}$. In particular, the selected half-shaft stiffness variation is less influential on controller performance than the variations of the torque generation time constant and drivetrain inertia; iv) the ranking in iii) is confirmed by the dimensional values of the comfort indicators, e.g., for $2\alpha = 1.2$ deg, $RMS_{\ddot{x}_b}$ with NMPC$^{(prev)}$ ranges from 0.049 m/s^2 for 'Variant A' to 0.251 m/s^2 for 'Variant D'; and v) at $2\alpha = 10$ deg, which represents an extreme and sub-optimal value of backlash, although not being able to generate benefits w.r.t. to the corresponding passive set-up because of the unmodeled dynamics of the simplified prediction model, NMPC$^{(prev)}$ does not imply any evident performance decrease for any considered drivetrain variant. This outcome – together with the observation in ii) – re-assures about the robustness of the implementation.

It was verified that the optimization of the cost function weights for each backlash magnitude – rather than for the minimum backlash value of the considered range – would not have provoked any substantial improvement of the results. However, these would have been characterised by a more linear behaviour, especially for $2\alpha = 6$ and 10 deg, i.e., with better KPI values for 6 deg backlash rather than 10 deg, while Fig. 15 – obtained with constant cost function weights – shows the opposite. The assumption of keeping the cost function weights constant along the vehicle operation – which brings a progressively increasing backlash value – is deemed to be the most realistic option, as in real vehicles the controller calibration is not currently varied according to the state of wear of the individual car.

In conclusion, the sensitivity analyses demonstrate the extent to which NMPC$^{(prev)}$ is effective, for a reasonably broad choice of on-board powertrain and drivetrain parameters, and therefore can be adapted to industrially available solutions.

5.5. *Effect of the electric motor time constant for '2 on-board'*

The objective is to assess how the '2 on-board' performance is influenced by the EM time constant, which has been demonstrated to have the highest impact among the considered parameters for the '4 on-board' configuration, see Fig. 14. The evaluation is conducted along the same road step test as in Section 5.2, which is repeated for '2 on-board' with the same time constant as for the nominal '4 on-board' case, i.e., $\tau_m = 5.7$ ms. The resulting profiles are depicted in Fig. 16, confirming the pre-emptive action capability to further mitigate the longitudinal acceleration oscillations, when coupled to faster EM response. Fig. 17 presents the percentage improvement of the KPIs for NMPC$^{(prev)}$ w.r.t. the passive case, for $\tau_m = 5.7$ ms and 25 ms. With the faster EM, all the longitudinal acceleration KPIs ($RMS_{\ddot{x}_b}$, $VDV_{\ddot{x}_b}$, and $\Delta\ddot{x}_{b,max}$) experience >59% reductions, while the root mean square value of the longitudinal jerk decreases by ~33%. In conclusion, by considering the likely advancements in EM actuation technology, it is reasonable to anticipate future performance improvements of the proposed control function, leveraging the most technologically advanced actuators.

5.6. *Asymmetric step road profile applied to '4 on-board' and '2 on-board' with equivalent parametrisations*

The simulations of this subsection investigate scenarios with an asymmetric road profile on the left and right EV sides. In the specific examples, the step profile of scenario 1 is shifted by $\Delta x_r = 0.25$ and 0.5 m between the right and left vehicle corners, from an initial speed $\dot{x}_{b,in} = 40$ km/h, at a total torque demand $T_{w,req} = 0$ Nm. To quantify the performance effect of the powertrain layout, the '4 on-board' and '2 on-board' cases are compared by assuming the same values ($\tau_m = 6$ ms, $J_{eq} =$ 2.8 kgm^2, and $2\alpha = 3.5$ deg) of the parameters that are mainly responsible for the system dynamics. For fairness of comparison, the J_{eq} values have been computed at the

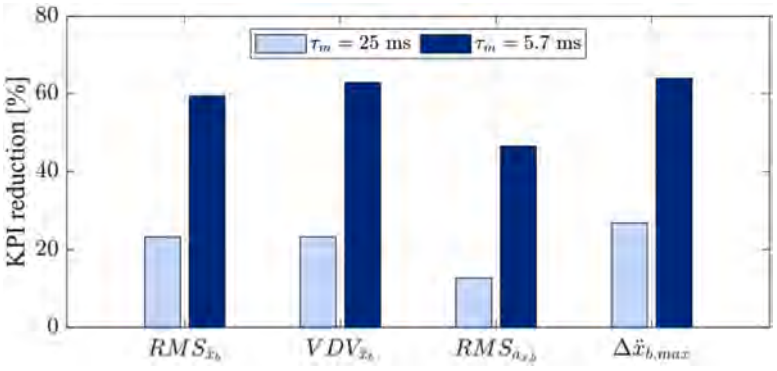

Fig. 17. KPI percentage reductions brought by NMPC$^{(prev)}$ w.r.t. the passive configuration for the '2 on-board' case. The analysis is conducted for two EM time constant values, for the symmetric road step test at zero torque demand, from an initial speed of 40 km/h.

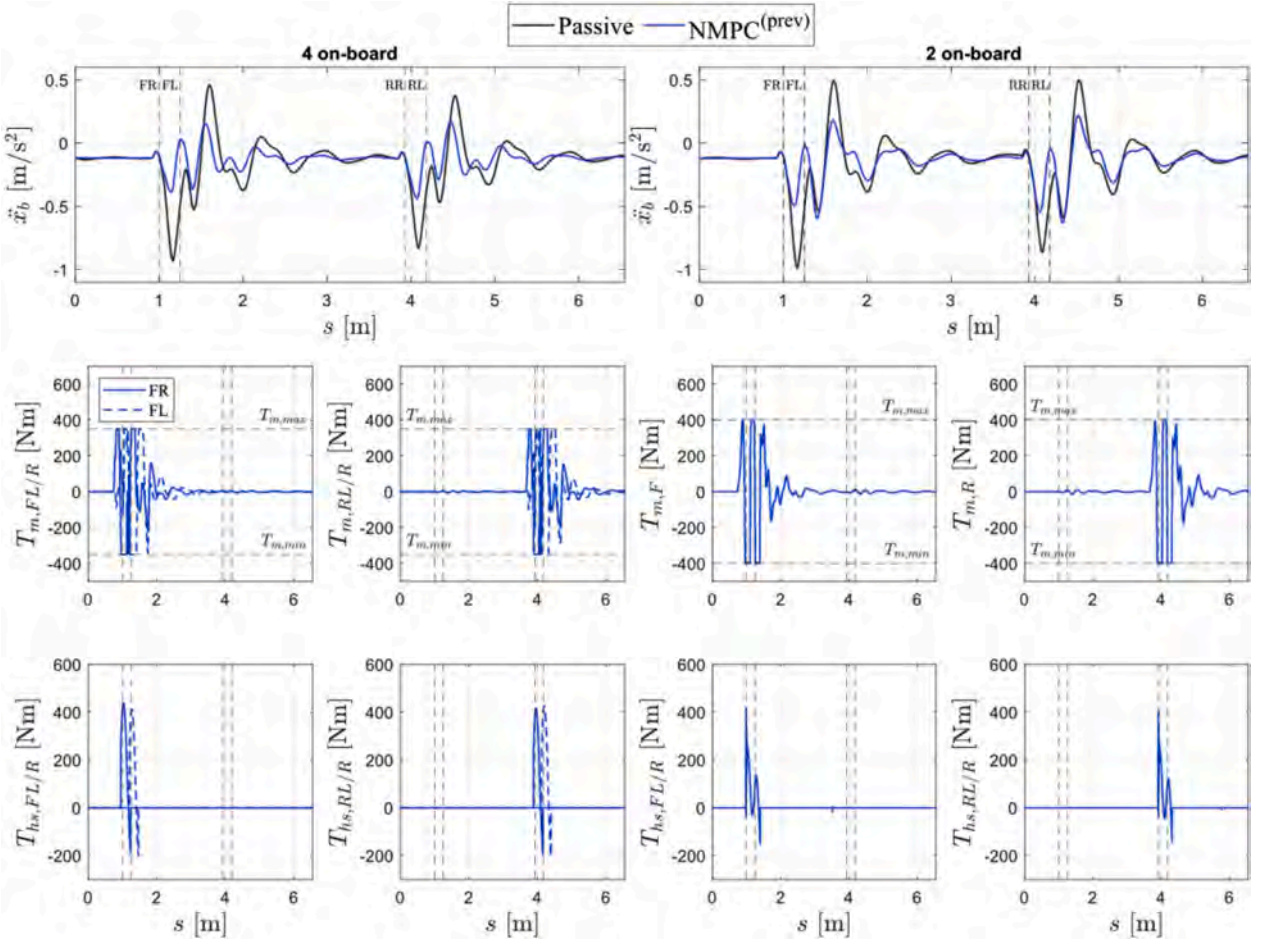

Fig. 18. Performance comparison of the passive and NMPC$^{(prev)}$ cases of the '4 on-board' and '2 on-board' configurations, along the considered asymmetric road step test ($\Delta x_r = 0.25$ m) at zero torque demand, from an initial speed of 40 km/h.

Table 3
KPI values for the considered controllers and powertrain configurations, for symmetric and asymmetric road excitations.

Configuration	4 on-board				2 on-board			
	$RMS_{\ddot{x}_b}$ [m/s^2]	$VDV_{\ddot{x}_b}$ [m/s$^{1.75}$]	$RMS_{\dot{a}_{x,b}}$ [m/s^3]	$\Delta\ddot{x}_{b,max}$ [m/s^2]	$RMS_{\ddot{x}_b}$ [m/s^2]	$VDV_{\ddot{x}_b}$ [m/s$^{1.75}$]	$RMS_{\dot{a}_{x,b}}$ [m/s^3]	$\Delta\ddot{x}_{b,max}$ [m/s^2]
Symmetry								
Passive	0.408	0.558	52.4	1.645	0.419	0.574	53.4	1.687
NMPC$^{(prev)}$	0.151	0.207	26.1	0.573	0.162	0.223	27.9	0.639
Asymmetry $\Delta x_r = 0.5$ m								
Passive	0.282	0.344	36.6	0.878	0.303	0.372	39.7	0.940
NMPC$^{(prev)}$	0.118	0.147	18.4	0.453	0.145	0.193	23.5	0.565
Asymmetry $\Delta x_r = 0.25$ m								
Passive	0.210	0.282	28.4	0.813	0.234	0.306	31.4	0.898
NMPC$^{(prev)}$	0.091	0. 119	18.6	0.365	0.141	0.187	23.6	0.513

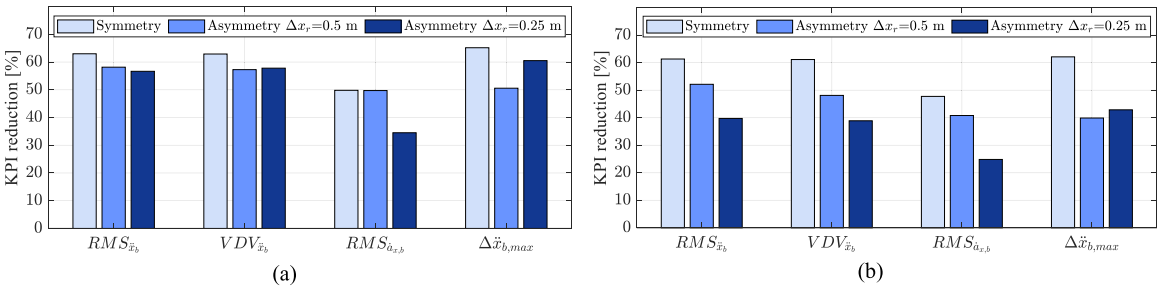

Fig. 19. KPI reductions brought by NMPC$^{(prev)}$ w.r.t the passive configuration, for: (a) '4 on-board'; and (b) '2 on-board'.

axle level, i.e., by considering the different number of powertrains per axle. The calibration weights have been optimized for each powertrain parametrization and road input scenario.

Fig. 18 plots the profiles of the main variables for $\Delta x_r = 0.25$ m, while Table 3 reports the KPIs in case of symmetric and asymmetric road excitations, for both powertrain configurations. For the same test cases, the KPI percentage reductions w.r.t the passive configuration are illustrated in Fig. 19. For all drivetrains and EM torque control set-ups, the acceleration-based KPIs are the highest for the symmetric road input test, followed – in order – by $\Delta x_r = 0.5$ m and $\Delta x_r = 0.25$ m. Through its independent wheel torque control, '4 on-board' with NMPC$^{(prev)}$ guarantees a rather consistent compensation level of the oscillations across the Δx_r values, with KPI reductions amounting to ~50%, see Fig. 19, with the exception of $RMS_{\dot{a}_{x,b}}$, which – although being more difficult to limit than the other indicators – decreases by at least 35%.

The reduction of the control performance benefit associated with the asymmetric input is more evident in '2 on-board'. In fact, because of the presence of a single motor per axle, the differential output torque is the same on the right and left side gears, and thus the central EM cannot tailor its response to the dynamics provoked by the asynchronous road excitations. For $\Delta x_r = 0.5$ m, the dynamics due to the right wheel excitations are almost exhausted before the left wheel excitations take over. Hence, when the distance shift is smaller, there is a greater overlap of the dynamics, and therefore the central motor struggles compensating for the effects of both excitations. Nevertheless, all reductions of the indicator values exceed 20% also for $\Delta x_r = 0.25$ m.

5.7. Controller evaluation on scenario 2

This section presents the results for scenario 2, i.e., the uneven profile of a typical ride comfort road, from an initial speed $\dot{x}_{b,in} = 40$ km/h, and a total torque demand $T_{w,req} = 0$ Nm. The cost function weights have been optimized for NMPC$^{(prev)}$ and the specific manoeuvre, while the tyre structure parameters of the prediction model have been modified to achieve a better match with the MF-Swift model along the considered road, rather than the step of Sections 5.1-5.5.

The resulting longitudinal acceleration and front and rear motor torque profiles are shown in Fig. 20, while the percentage improvement of the KPIs for NMPC$^{(w/o\ prev)}$ and NMPC$^{(prev)}$ w.r.t. the passive case are in Fig. 21. For 'In-wheel' and '4 on-board', NMPC$^{(prev)}$ achieves a significant enhancement w.r.t. the passive EV, e.g., see the accelerations immediately before and after 15 m, where the pre-emptive action on the motor torque brings a major attenuation of the peaks. However, also NMPC$^{(w/o\ prev)}$ still provides evident benefits, especially for the 'In-wheel' configuration. For '2 on-board', the slowness in the drivetrain system response to such aggressive road profile makes the improvement associated with NMPC$^{(prev)}$ marginal and evident only in terms of attenuation of the acceleration peaks, e.g., see those between 34 m and 39 m. From the KPI perspective, NMPC$^{(w/o\ prev)}$ reduces the acceleration-related indicators from ~25% to >40% for the 'In-wheel' and '4 on-board' configurations, while for '2 on-board' no improvement can be

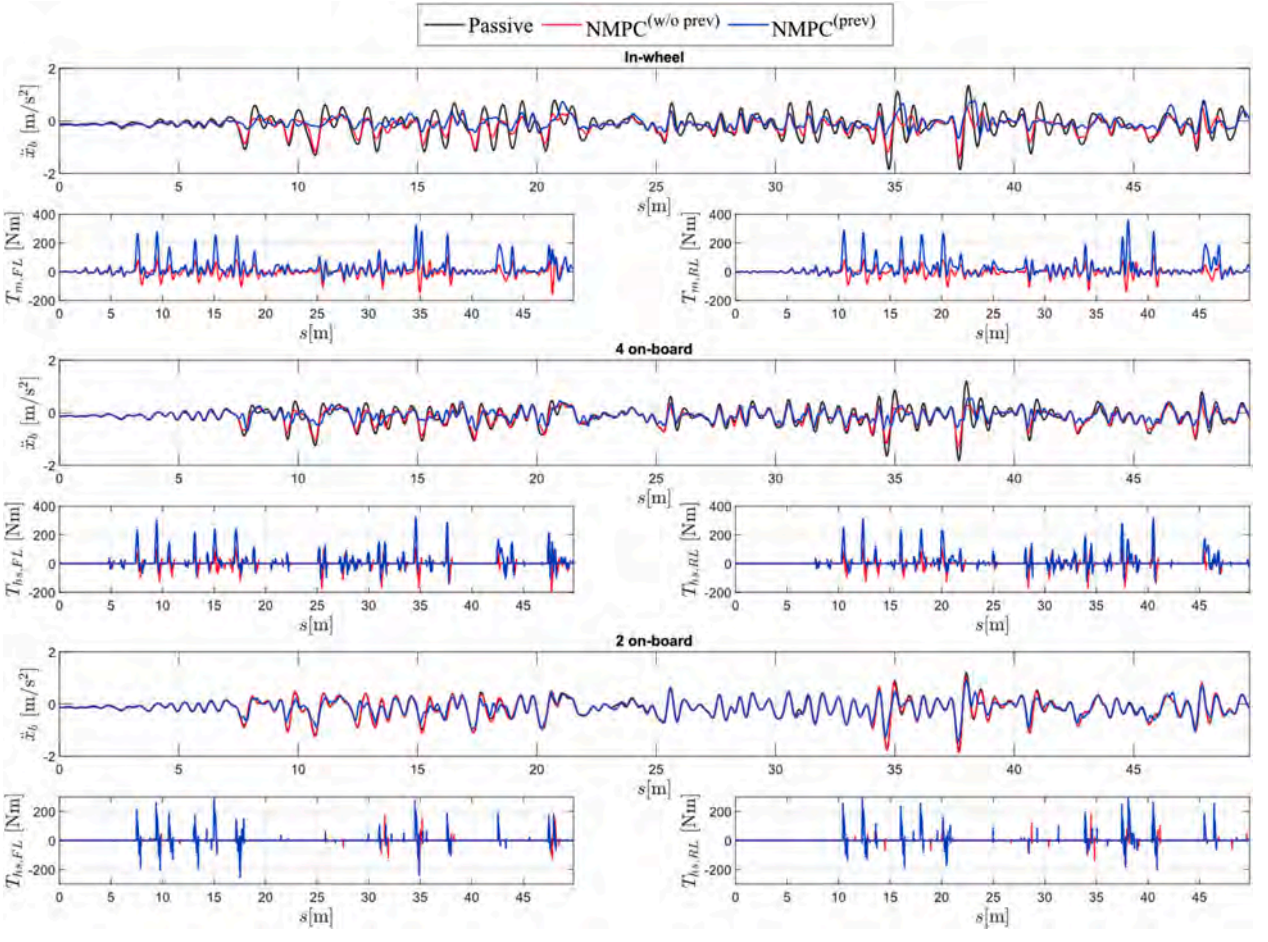

Fig. 20. Controller performance comparison on a typical ride comfort road profile starting from an initial speed of 40 km/h.

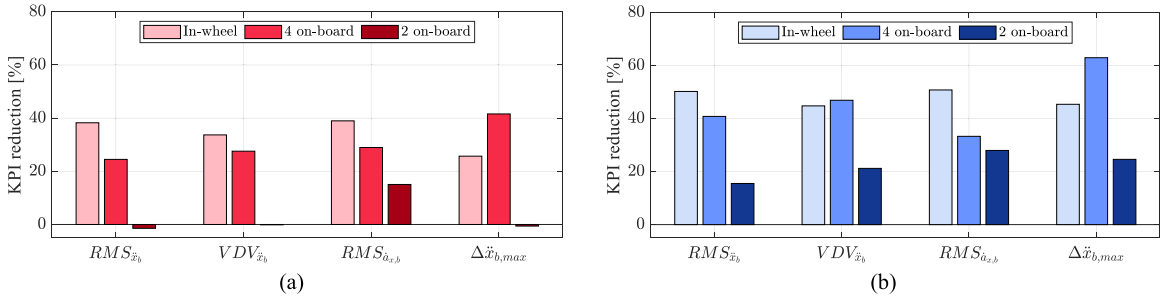

Fig. 21. KPI reductions brought by (a) NMPC$^{(w/o\ prev)}$ and (b) NMPC$^{(prev)}$ w.r.t. the passive configuration for the test in Fig. 15.

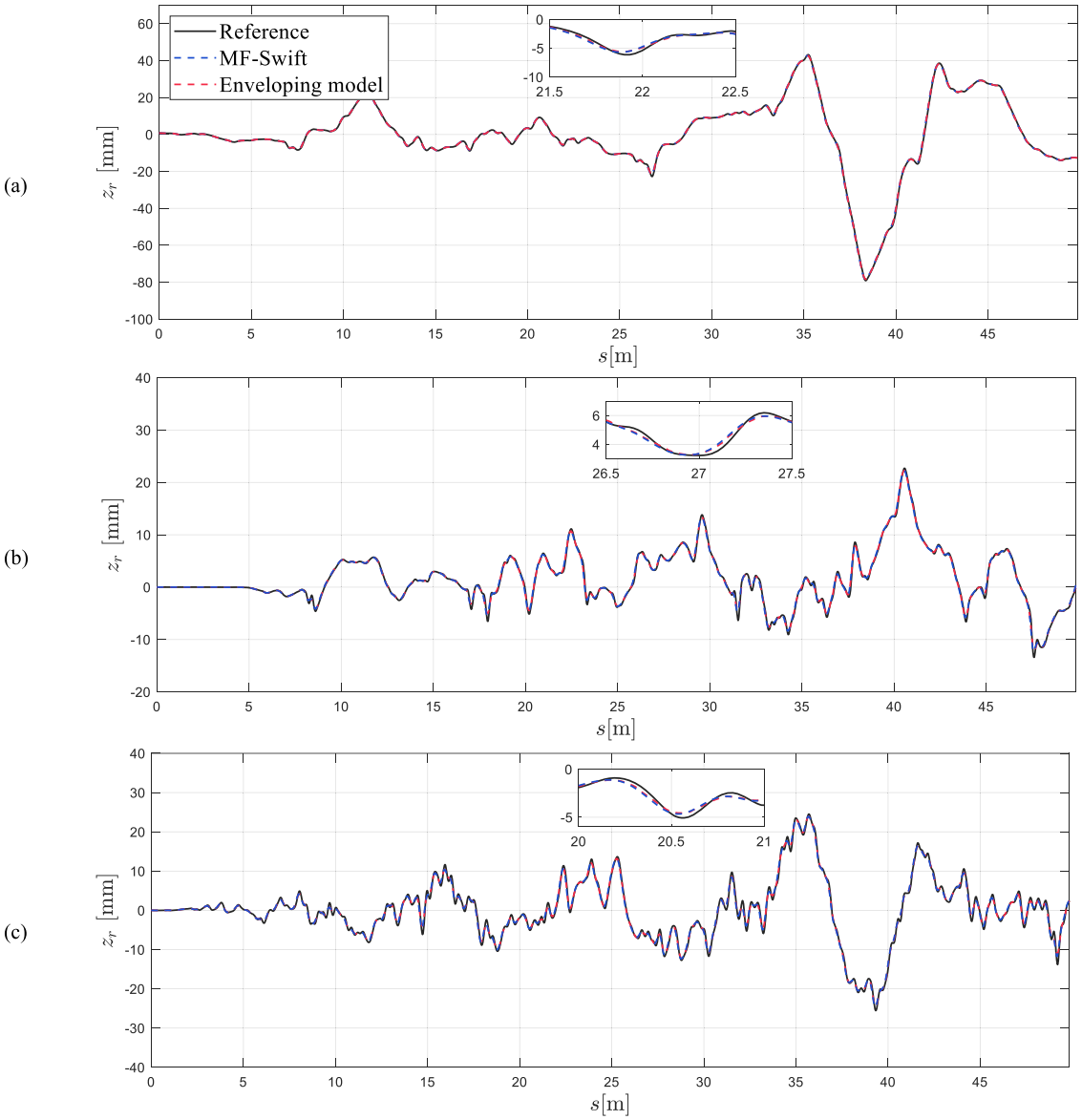

Fig. 22. Comparison of the actual road profiles (Reference), MF-Swift tyre model filtered profiles (MF-Swift), and control-oriented enveloping tandem model profiles (Enveloping model) for (a) scenario 3; (b) scenario 4; and (c) scenario 5.

Table 4
KPI percentage improvement w.r.t. the passive configurations for the '4 on-board' case along different road profiles.

Scenario	Road class	Configuration	4 on-board			
			$RMS_{\ddot{x}_b}$ [m/s^2]	$VDV_{\ddot{x}_b}$ [m/s$^{1.75}$]	$RMS_{\dot{a}_{x,b}}$ [m/s^3]	$\Delta\ddot{x}_{b,max}$ [m/s^2]
		$\dot{x}_{b,in} = 40$ km/h				
3	Class A	Passive	0.179	0.247	14.1	0.960
	$G_d(\Omega_0) = 0.8\ 10^{-6}$ m^3/rad	NMPC$^{(w/o\ prev)}$	0.148	0.203	12.8	0.878
		NMPC$^{(prev)}$	0.120	0.143	12.9	0.482
4	Class A	Passive	0.169	0.203	18.8	0.740
	$G_d(\Omega_0) = 1.5\ 10^{-6}$ m^3/rad	NMPC$^{(w/o\ prev)}$	0.136	0.169	18.7	0.697
		NMPC$^{(prev)}$	0.119	0.147	17.4	0.565
5	Class B	Passive	0.320	0.398	36.1	1.365
	$G_d(\Omega_0) = 3\ 10^{-6}$ m^3/rad	NMPC$^{(w/o\ prev)}$	0.232	0.274	32.4	0.912
		NMPC$^{(prev)}$	0.206	0.246	31.7	0.819

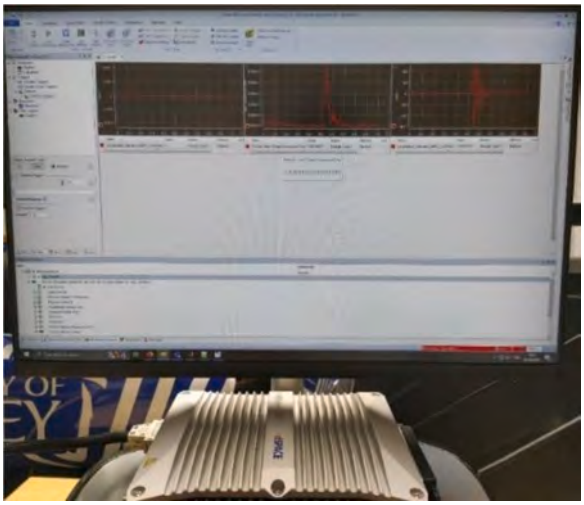

Fig. 23. Real-time implementation of the proposed controllers on a dSPACE MicroAutoBox III unit.

observed w.r.t. the passive case (on the contrary, $RMS_{\ddot{x}_b}$ and $\Delta\ddot{x}_{b,max}$ very slightly worsen), except for $RMS_{\dot{a}_{x,b}}$ that is reduced by ~15%. On the contrary, NMPC$^{(prev)}$ consistently improves the KPIs for all configurations by ~15 to 25% w.r.t. NMPC$^{(w/o\ prev)}$, and thus implies that also the controlled '2 on-board' case performs consistently better than the passive EV.

5.8. Sensitivity analysis on different road profiles for '4 on-board'

The scope of this analysis is to highlight the capability of the NMPC for the '4 on-board' configuration to operate effectively on a selection of road profiles. Hence, additional simulations are conducted on the ride comfort road profiles illustrated in Figs. 22(a)-(c), referred to as scenarios 3-5. These profiles are categorized in accordance with ISO 8608 [60], based on the power spectral density of the vertical road displacement, denoted as $G(\Omega_0)$, where Ω_0 is the reference spatial frequency ($\Omega_0 = 1$ rad/m for a frequency $n_0 = 1/2\pi$ cycles/m with wavelength $L_0 = 6.28$ m) [61]. Based on this classification, scenarios 2 ($G_d(\Omega_0) = 5\ 10^{-6}$ m^3/rad) and 5 ($G_d(\Omega_0) = 3\ 10^{-6}$ m^3/rad) fall within the road class B, while scenarios 3 ($G_d(\Omega_0) = 0.8\ 10^{-6}$ m^3/rad) and 4 ($G_d(\Omega_0) = 1.5\ 10^{-6}$ m^3/rad) within category A. Road classes A and B represent typical road profiles, and are largely used for ride comfort analyses [61]. The KPI values for scenarios 3-5, presented in Table 4, confirm the trends already observed for Scenario 2, i.e., NMPC$^{(prev)}$ consistently outperforms the other configurations.

6. Real-time implementation and preliminary proof-of-concept experiments

6.1. Preliminary real-time implementation

To verify their capability to run in real-time with currently available control hardware, the proposed proof-of-concept NMPCs were deployed on a rapid control prototyping unit, i.e., a dSPACE MicroAutoBox III system (1.4 GHz, 64 Mb flash memory), see Fig. 23 (more powerful control units are already on the market, and further significant progress is expected soon). The selected combinations

Fig. 24. (a) The ZEBRA vehicle of the University of Surrey equipped with a Racelogic VBOX3i dual GPS system; (b) wire suspension displacement and wheel speed sensors installed at the rear-left corner; and (c) the dSPACE MicroAutoBox II rapid control prototyping unit of the vehicle.

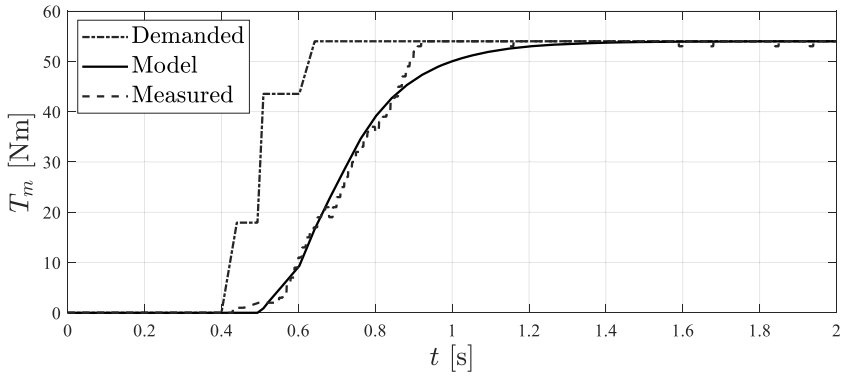

Fig. 25. Profiles of the reference motor torque (Demanded), modelled motor torque (Model), and actual motor torque obtained from the experimentally measured motor current (Measured) along a torque step test.

of sampling time t_s, number of prediction steps N_h, and solver iterations N_{iter} that ensure real-time operation are: i) $t_s = 3$ ms, $N_h = 9$, and $N_{iter} = 2$, for 'In-wheel'; ii) $t_s = 4$ ms, $N_h = 7$, and $N_{iter} = 2$, for '4 on-board'; and iii) $t_s = 6$ ms, $N_h = 7$, and $N_{iter} = 1$, for '2 on-board'. In i)-iii), the discretization time of the prediction models were set to be half of the corresponding sampling time, which ensures a good trade-off between numerical stability and computational effort.

The real-time settings of the controllers were assessed through simulations along the test of Section 5.2. The corresponding KPIs are reported in bold in Table 2. Despite the larger sampling time and lower number of prediction steps w.r.t. the previous simulation-oriented NMPC versions, for all three drivetrain layouts the real-time NMPC$^{(\text{prev})}$ configuration ensures an evident improvement w. r.t. the passive case. For example, $RMS_{\ddot{x}_b}$, $VDV_{\ddot{x}_b}$, $\Delta\ddot{x}_{b,max}$, and $RMS_{\dot{a}_{x,b}}$ of NMPC$^{(\text{prev})}$ are reduced by a factor >2 for '4 on-board'. For the slower '2 on-board' configuration, the results highlight a general enhancement of the KPIs, with the exception of $RMS_{\dot{a}_{x,b}}$, which,

however, was not part of the optimisation associated with the calibration cost function J_{WT}. It was also verified that a more responsive set-up of the '2 on-board' powertrain configuration, with $\tau_m = 5.7$ ms, would have enabled an evident jerk indicator reduction for the real-time setting of the controller. The promising results of the real-time algorithms highlight the potential of the proposed proof-of-concept preview-based solution to be implemented at a higher technology readiness level in follow-up studies.

6.2. Experimental vehicle testing set-up

Preliminary experimental vehicle tests were conducted on the prototype Zero Emission test Bed for Research on Autonomous driving (ZEBRA) of the University of Surrey. ZEBRA is a modified Renault Twizy, i.e., an L7e rear-wheel-drive electric quadricycle with a centralized on-board electric powertrain with single-speed transmission and open differential. The vehicle is equipped with: i) a set of conventional vehicle dynamics sensors, e.g., wheel speed sensors; ii) wire displacement sensors to measure the suspension travel of each corner; iii) a Racelogic VBOX3i dual GPS (global positioning system) with a fixed base location for precise localisation; and iv) a dSPACE MicroAutoBox II system – significantly less powerful than the one used in Section 6.1 – for the rapid prototyping of the proposed comfort-oriented control function. Fig. 24 shows the vehicle testing set-up, i.e., the ZEBRA vehicle and its associated equipment in testing conditions. The transient response of the ZEBRA powertrain was validated through tip-in tests, i.e., step-like torque demand tests, see Fig. 25. The validation plot highlights the extremely slow motor torque response, which can be well approximated by a pure time delay of ~100 ms, followed by a first order model with a time constant τ_m of ~160 ms, see the 'Model' line in the figure.

The controller formulation of Section 3.2 was adapted to the specific rear-wheel-drive EV architecture, and simplified for the real-time operation with the available control hardware. The implemented simplifications involved: i) considering a rigid direct drive powertrain design in the prediction model, which neglects the behaviour of the open differential internals, and the torsional dynamics of the half-shafts; and ii) using a prediction horizon of 200 ms with a variable discretization approach, i.e., including 4 prediction steps at 10 ms, followed by 4 steps at 50 ms. The relatively long prediction horizon is required to meaningfully account for the low powertrain responsiveness within the prediction. To address the pure time delay, the preview information of the effective road profile was supplied to the algorithm with an offset equal to the pure time delay of the powertrain torque response.

6.3. Preliminary proof-of-concept experimental results

The preliminary proof-of-concept experimental tests were performed in the autonomous driving mode of the ZEBRA vehicle. The maximum torque request was applied to accelerate the vehicle up to the target speed of 30 km/h; subsequently, the traction torque demand was released, down to a marginally negative value, and the vehicle traversed a 3 cm high and 25 cm long speed bump. Fig. 26 shows photographic frames from the implemented experimental scenario. The plots of the experimental results, focusing on the section of the test in which the rear wheels encounter the speed bump (indicated by the grey area in the subplots), are presented in Fig. 27, which includes the profiles of the longitudinal acceleration and speed of the vehicle (computed from the measured speed of the front left undriven wheel, hence the notations $\ddot{x}_{b,\omega_{FL}}$ and $\dot{x}_{b,\omega_{FL}}$), the rear left suspension travel, and the NMPC$^{(prev)}$ torque correction, as a function of the travelled distance, s. Despite the extremely slow motor response, the road preview information allows the controller to more than halve the longitudinal acceleration and speed oscillations, by requesting a control action well in advance, with a significantly increased damping level. The benefit is also evident in the third subplot, where the vertical component of the driving force reduces the rear left suspension travel. In summary, these results are very promising, especially when considering the very slow dynamics of the specific electric powertrain, which would suggest an even more evident performance benefit of the proposed control function with more performing powertrains.

7. Conclusions

This study presented novel proof-of-concept nonlinear model predictive control (NMPC) algorithms to attenuate the longitudinal acceleration oscillations caused by irregular road profiles. Based on the road preview information, the NMPC$^{(prev)}$ strategies modulate the reference torque sent to the inverters of the on-board electric powertrains of the considered four-wheel-drive electric vehicle configurations with one or two electric machines per axle, respectively referred to as '2 on-board' and '4 on-board'. The preliminary results, obtained through simulations with an experimentally validated vehicle model, and including comparisons with those associated with a more reactive in-wheel direct drive powertrain configuration, referred to as 'In-wheel', bring the following conclusions:

- If optimized for the considered symmetric positive step input test, NMPC$^{(prev)}$ achieves excellent compensation of the longitudinal acceleration oscillations, by reducing the related key performance indicators (KPIs) by >82% for the '4 on-board' configuration, w.r.t. the passive case. Also in the more challenging '2 on-board' layout with slower motor response and larger drivetrain backlash, NMPC$^{(prev)}$ achieves a ~24% improvement of the acceleration-related indicators. The algorithm is effective for a wide range of vehicle speeds and motor torque demands.
- The sensitivity analyses along the step test with different system parameters, i.e., motor time constant, equivalent drivetrain inertia, half-shaft stiffness, and equivalent drivetrain backlash, demonstrate the controller ability to perform well for a wide range of industrially available electric powertrain solutions, with different bandwidths and dynamic torque response characteristics, for localized and symmetric road inputs. For example, when quadrupling the torque generation time constant of the electric machine of

Fig. 26. Frames of the ZEBRA vehicle captured during the speed bump test.

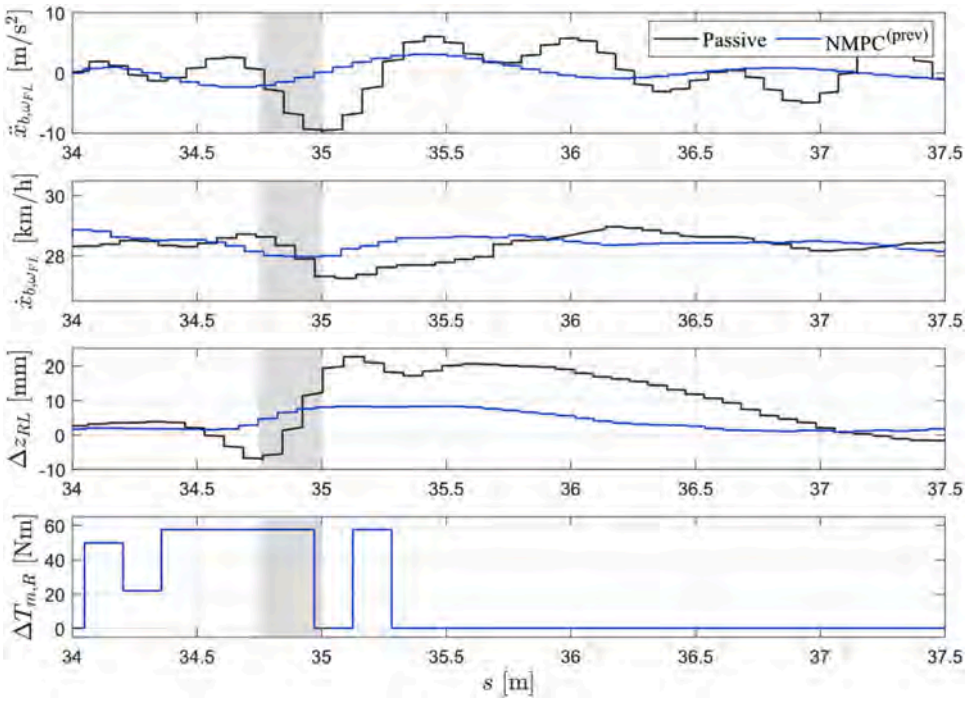

Fig. 27. Experimental comparison of the passive and NMPC$^{(prev)}$ configurations of the ZEBRA vehicle, along the considered speed bump test from an initial speed of ~30 km/h (the grey area approximately indicates when the rear axle encounters the speed bump).

'4 on-board', NMPC$^{(prev)}$ still guarantees a ~65% attenuation of the root mean square value of the longitudinal acceleration error w.r.t. the passive case.

- The step test with asymmetric road inputs demonstrates that the solutions with independent torque control on the single wheel, i.e., 'In-wheel' and '4 on-board', can achieve rather consistent performance independently from the difference between the road profiles on the left and right sides. On the contrary, although still providing evident benefits, '2 on-board' is affected by the left-to-right profile difference, since such powertrain architecture can inherently generate only a torque profile that is a compromise among the requirements on the two vehicle sides.
- Although with dedicated retuning, the NMPC formulations confirm their potential on the selected ride comfort road. For the 'In-wheel' and '4 on-board' configurations, the controller version without road preview, i.e., NMPC$^{(w/o\ prev)}$, reduces the KPIs from ~25% to >40%, while no evident benefit is achieved for the more critical '2 on-board' set-up. The inclusion of road preview further improves all indicators by ~20%, which makes NMPC$^{(prev)}$ a convenient solution for all considered architectures, including '2 on-board'.
- In spite of the proof-of-concept nature of the simulation-based analysis, NMPC$^{(prev)}$ is real-time implementable on currently available control hardware, and its real-time settings imply only marginal performance decrease w.r.t. the optimised simulation-oriented controller parametrisations.

Despite the slow time response of the electric motor torque in the selected demonstrator vehicle, proof-of-concept experimental results confirm the capability of NMPC$^{(prev)}$ to significantly reduce the longitudinal acceleration oscillations, underscoring its versatility as an effective solution for on-board drivetrain architectures.

Future developments will include: i) comprehensive experimental demonstrations of the algorithms on physical vehicle demonstrators with in-wheel and on-board powertrains; ii) the implementation of the state estimation and sensing system required to experimentally deploy the controllers at higher technology readiness levels; iii) the design and evaluation of alternative data-driven prediction models, e.g., using deep neural networks, to replace the physics-based formulations, and target enhanced matching with the plant dynamics as well as lower computational effort; and iv) the development of further road-preview based control functionalities, e.g., anti-jerk and traction controllers, based on the prediction model of this research.

CRediT authorship contribution statement

Pietro Stano: Writing – original draft, Validation, Software, Methodology, Investigation, Formal analysis, Data curation, Conceptualization. **Davide Lazzarini:** Writing – original draft, Visualization, Validation, Software, Methodology, Investigation. **Silvio Santoro:** Writing – original draft, Visualization, Validation, Software, Formal analysis. **Mario Mihalkov:** Validation, Data curation. **Umberto Montanaro:** Writing – review & editing, Supervision, Investigation, Formal analysis, Conceptualization. **Alessandro**

Vigliani: Writing – review & editing, Supervision, Methodology, Funding acquisition, Formal analysis, Data curation, Conceptualization. **Antonella Ferrara:** Writing – review & editing, Supervision, Methodology, Funding acquisition, Conceptualization. **Miguel Dhaens:** Writing – review & editing, Validation, Resources, Funding acquisition, Data curation, Conceptualization. **Aldo Sorniotti:** Writing – review & editing, Writing – original draft, Supervision, Resources, Project administration, Methodology, Investigation, Funding acquisition, Formal analysis, Conceptualization.

Declaration of competing interest

The authors declare the following financial interests/personal relationships which may be considered as potential competing interests:

Aldo Sorniotti reports financial support was provided by European Commission. If there are other authors, they declare that they have no known competing financial interests or personal relationships that could have appeared to influence the work reported in this paper.

Data availability

Data will be made available on request.

Acknowledgements

This work was supported by the Horizon 2020 Programme of the European Commission under Grant agreement numbers 824250 (EVC1000 project), 872907 (OWHEEL project), and 101096083 (EM-TECH project).

References

[1] L. Castellazzi, A. Tonoli, N. Amati, Piu, E Galliera, Vehicle Driveability: Dynamic Analysis of Powertrain System Components, SAE Technical Papers (2016), https://doi.org/10.4271/2016-01-1124.
[2] R. Burdzik, Identification of structure and directional distribution of vibration transferred to car-body from road roughness, J. Vibroengineering 16 (1) (2014) 324–333.
[3] Prażnowski, K. and Mamala, J. (2017). Problems in Assessing Pneumatic Wheel Unbalance of a Passenger Car Determined with Test Road in Normal Conditions. SAE Technical Paper 2017-01-1805. https://doi.org/10.4271/2017-01-1805.
[4] J.J. Zhu, A. Khajepour, E. Esmailzadeh, A. Kasaiezadeh, Ride quality evaluation of a vehicle with a planar suspension system, Vehicle Syst. Dyn. 50 (3) (2012) 395–413, https://doi.org/10.1080/00423114.2011.592591.
[5] Z. Guo, W. Wu, S. Yuan, Longitudinal-vertical dynamics of wheeled vehicle under off-road conditions, Vehicle Syst. Dyn. 60 (2) (2022) 470–490, https://doi.org/10.1080/00423114.2020.1823003.
[6] T. Beauduin, S. Yamada, H. Fujimoto, T. Kanou, E. Katsuyama, Control-oriented modelling and experimental modal analysis of Electric Vehicles with geared In-Wheel Motors, in: IEEE/ASME Conference on Intelligent Advanced Mechatronics, 2017, pp. 541–546, https://doi.org/10.1109/AIM.2017.8014073.
[7] L. Levulyte, V. Žuraulis, E. Sokolovskij, The impact of road roughness on the duration of contact between a vehicle wheel and road surface, Transport 29 (4) (2014) 430–438, https://doi.org/10.3846/16484142.2014.984330.
[8] E. Tseng, D Hrovat, State of the art survey: Active and semi-active suspension control, Vehicle Syst. Dyn. 53 (7) (2015) 1034–1062, https://doi.org/10.1080/00423114.2015.1037313.
[9] X. Wu, Y. Pan, G. Wang, L. Hou, Pitch motion suppression of electric vehicle active suspensions based on multibody dynamics, Mech. Mach. Theory. 198 (2024) 105667, https://doi.org/10.1016/j.mechmachtheory.2024.105667.
[10] A. Ugenti, R. Galati, G. Mantriota, G Reina, Analysis of an all-terrain tracked robot with innovative suspension system, Mech. Mach. Theory. 182 (2023) 105237, https://doi.org/10.1016/j.mechmachtheory.2023.105237.
[11] J. Theunissen, A. Tota, P. Gruber, M. Dhaens, A. Sorniotti, Preview-based techniques for vehicle suspension control: a state-of-the-art review, Annu Rev. Control 51 (2021) 206–235, https://doi.org/10.1016/j.arcontrol.2021.03.010.
[12] N. Hamadi, D. Ameddah, H. Imine, Investigation of the Adherence Influence on the Dynamic Behavior of the Vehicle, International Journal of Hybrid Information Technology 7 (5) (2014) 85–102, https://doi.org/10.14257/ijhit.2014.7.5.08.
[13] N. Ezra, A. Cohen, D Zarrouk, Modeling, simulation, and experiments of a flexible track robot over rigid horizontal and inclined surfaces, Mech. Mach. Theory. 199 (2024) 105689, https://doi.org/10.1016/j.mechmachtheory.2024.105689.
[14] S. Murata, Innovation by in-wheel-motor drive unit, Vehicle Syst. Dyn. 50 (6) (2012) 807–830, https://doi.org/10.1080/00423114.2012.666354.
[15] T. Kobayashi, E. Katsuyama, H. Sugiura, E. Ono, M. Yamamoto, Direct yaw moment control and power consumption of in-wheel motor vehicle in steady-state turning, Vehicle Syst. Dyn. 55 (1) (2017) 104–120, https://doi.org/10.1080/00423114.2016.1246737.
[16] A. Watts, A. Vallance, A. Whitehead, C. Hilton, A. Fraser, The Technology and Economics of In-Wheel Motors, SAE International Journal of Passenger Cars – Electronic and Electrical Systems 3 (2) (2010) 37–57, https://doi.org/10.4271/2010-01-2307.
[17] S. Derammelaere, M. Haemers, J. De Viaene, F. Verbelen, K. Stockman, A quantitative comparison between BLDC, PMSM, brushed DC and stepping motor technologies, in: 19th International Conference on Electrical Machines and Systems (ICEMS), 2016, pp. 1–5.
[18] Y. Qin, Z. Zhao, Z. Wang, G. Li, Study of Longitudinal–Vertical Dynamics for In-Wheel Motor-Driven Electric Vehicles, Automot. Innov. 4 (2021) 227–237, https://doi.org/10.1007/s42154-021-00141-5.
[19] Chen, L., Zhang, S., Bian, M., Luo, Y., and Li, K. (2016). An Explanation of the In-Wheel Motor Drive System's Vibration at Low Velocity Using Motor-Wheel Frequency Characteristics. SAE Technical Paper 2016-01-1673. https://doi.org/10.4271/2016-01-1673.
[20] M. Yu, Z. Shuguang, W. Xudong, D Xianglei, High frequency vibration characteristics of electric wheel system under in-wheel motor torque ripple, J. Sound. Vib. 400 (2017) 42–456, https://doi.org/10.1016/j.jsv.2017.04.011.
[21] D. Mohanraj, J. Gopalakrishnan, B. Chokkalingam, L. Mihet-Popa, Critical Aspects of Electric Motor Drive Controllers and Mitigation of Torque Ripple—Review, IEEe Access. 10 (2022) 73635–73674, https://doi.org/10.1109/ACCESS.2022.3187515.
[22] M. Polat, A. Yildiz, R Akinci, Performance Analysis and Reduction of Torque Ripple of Axial Flux Permanent Magnet Synchronous Motor Manufactured for Electric Vehicles, IEEE Transactions on Magnetics 57 (7) (2021) 1–9, https://doi.org/10.1109/TMAG.2021.3078648.
[23] H. Zhang, M. Yang, Y. Zhang, J. Tuo, S. Luo, J. Xu, Analytical calculation of surface-inset PM in-wheel motors and reduction of torque ripple, IEEE Transactions on Magnetics 57 (1) (2020) 1–11, https://doi.org/10.1109/TMAG.2020.3034882.

[24] Z. Zhao, H. Taghavifar, H. Du, Y. Qin, M. Dong, L. Gu, In-Wheel Motor Vibration Control for Distributed-Driven Electric Vehicles: A Review, IEEE Transactions on Transportation Electrification 7 (4) (2021) 2864–2880, https://doi.org/10.1109/TTE.2021.3074970.

[25] A.A. Ahmed, A. Alsharif, T. Triwiyanto, M. Khaleel, C.W. Tan, R Ayop, Using of Neural Network-Based Controller to Obtain the Effect of Hub Motors Weight on Electric Vehicle Ride Comfort, in: IEEE 2nd International Maghreb Meeting of the Conference on Sciences and Techniques of Automatic Control and Computer Engineering (MI-STA), 2022, pp. 189–192, https://doi.org/10.1109/MI-STA54861.2022.9837608.

[26] L. Jin, Y. Yu, Y. Fu, Study on the ride comfort of vehicles driven by in-wheel motors, Advances in Mechanical Engineering 8 (3) (2016), https://doi.org/10.1177/1687814016633622.

[27] H. Salmani, M. Abbasi, T. Fahimi Zand, M. Fard, R. Nakhaie Jaza, A new criterion for comfort assessment of in-wheel motor electric vehicles, Journal of Vibration and Control 28 (3-4) (2022) 316–328, https://doi.org/10.1177/1077546320977187.

[28] X. Shao, F. Naghdy, H. Du, Y. Qin, Coupling effect between road excitation and an in-wheel switched reluctance motor on vehicle ride comfort and active suspension control, J. Sound. Vib. 443 (2019) 683–702, https://doi.org/10.1016/j.jsv.2018.12.012.

[29] I. Bakirci, N. Katadzic, The use of wheel torque modulation to mitigate road induced longitudinal vibrations, Dept. Appl. Mechanics. Chalmers Univ. Technol., Göteborg, Sweden, 2014. M.Sc. thesis.

[30] H. Fukudome, Reduction of Longitudinal Vehicle Vibration Using In-Wheel Motors, SAE Int., 2016, https://doi.org/10.4271/2016-01-1668.

[31] F. Walz, S. Hohmann, On model-based longitudinal feed-forward motion control for low velocities on known road profiles, Vehicle Syst. Dyn. 57 (8) (2018) 1126–1142, https://doi.org/10.1080/00423114.2018.1498111.

[32] F. Walz, S. Hohmann, Model predictive longitudinal motion control for low velocities on known road profiles, Vehicle Syst. Dyn. 58 (8) (2019) 1310–1328, https://doi.org/10.1080/00423114.2019.1618880.

[33] S. Yamada, T. Beauduin, H. Fujimoto, T. Kanou, E. Katsuyama, Model-based longitudinal vibration suppression control for electric vehicles with geared in-wheel motors, in: IEEE Conference on Intelligent Advanced Mechatronics, 2017, pp. 517–522, https://doi.org/10.1109/AIM.2017.8014069.

[34] S. Yamada, T. Beauduin, H. Fujimoto, T. Kanou, E. Katsuyama, Active Model-Based Suppression of Secondary Ride for Electric Vehicles With In-Wheel Motors, IEEE/ASME Transactions on Mechatronics 27 (6) (2022) 5637–5646, https://doi.org/10.1109/TMECH.2022.3187414.

[35] J. Theunissen, A. Sorniotti, P. Gruber, S. Fallah, M. Ricco, M. Kvasnica, M. Dhaens, Regionless Explicit Model Predictive Control of Active Suspension Systems With Preview, IEEE Transactions on Industrial Electronics 67 (6) (2020) 4877–4888, https://doi.org/10.1109/TIE.2019.2926056.

[36] V. Vidal, P. Stano, G. Tavolo, M. Dhaens, D. Tavernini, P. Gruber, A. Sorniotti, On Pre-Emptive In-Wheel Motor Control for Reducing the Longitudinal Acceleration Oscillations Caused by Road Irregularities, IEEe Trans. Veh. Technol. 71 (9) (2022) 9322–9337, https://doi.org/10.1109/TVT.2022.3172172.

[37] F. Bottiglione, A. Sorniotti, L. Shead, The effect of half-shaft torsion dynamics on the performance of a traction control system for electric vehicles, Proceedings of the Institution of Mechanical Engineers Part D Journal of Automobile Engineering 226 (9) (2012) 1145–1159, https://doi.org/10.1177/0954407012440526.

[38] J. Zhang, B. Chai, X. Lu, Active oscillation control of electric vehicles with two-speed transmission considering nonlinear backlash, Proceedings of the Institution of Mechanical Engineers, Part K Journal of Multi-body Dynamics 234 (1) (2020) 116–133, https://doi.org/10.1177/1464419319877332.

[39] M. Canova, C. Rostiti, L. D'Avico, S. Stockar, G. Chen, M. Prucka, H. Dourra, Model-Based Wheel Torque and Backlash Estimation for Drivability Control, SAe Int. J. Engines. 10 (3) (2017) 1318–1327, https://doi.org/10.4271/2017-01-1111.

[40] A. Scamarcio, C. Caponio, M. Mihalkov, P. Georgiev, J. Ahmadi, K.M. So, D. Tavernini, A. Sorniotti, Predictive anti-jerk and traction control for V2X connected electric vehicles with central motor and open differential, IEEe Trans. Veh. Technol. 72 (6) (2022) 7221–7239, https://doi.org/10.1109/TVT.2022.3143497.

[41] A.M. Dizqah, B. Lenzo, A. Sorniotti, P. Gruber, S. Fallah, J De Smet, A Fast and Parametric Torque Distribution Strategy for Four-Wheel-Drive Energy-Efficient Electric Vehicles, IEEE Transactions on Industrial Electronics 63 (7) (2016) 4367–4376, https://doi.org/10.1109/TIE.2016.2540584.

[42] A. Parra, D. Tavernini, P. Gruber, A. Sorniotti, A. Zubizarreta, J. Pérez, On Nonlinear Model Predictive Control for Energy-Efficient Torque-Vectoring, IEEe Trans. Veh. Technol. 70 (1) (2021) 173–188, https://doi.org/10.1109/TVT.2020.3022022.

[43] S. De Pinto, P. Camocardi, C. Chatzikomis, A. Sorniotti, F. Bottiglione, G. Mantriota, P. Perlo, On the Comparison of 2- and 4-Wheel-Drive Electric Vehicle Layouts with Central Motors and Single- and 2-Speed Transmission Systems, Energies. (Basel) 13 (13) (2020) 3328, https://doi.org/10.3390/en13133328.

[44] Siemens Digital Industries Software, (2020.2). Simcenter Tire – MF-Tyre/MF-Swift User Manual.

[45] Armengaud, E., Hegazy, O., Brandstatter, B., Ivanov, V., Tatschl, R., De Gennaro, M., Sorniotti, A., Mierlo, J., and Schernus, C. (2019). European Innovation for Next Generation Electrified Vehicles and Components. 1-6. https://doi.org/10.1109/ICCVE45908.2019.8964843.

[46] Alessandro. Scamarcio, Active systems for drivability improvement of electric vehicles, School of Mechanical Engineering Sciences, University of Surrey, Guildford, UK, 2020. Ph.D. thesis.

[47] E. Galvagno, M. Velardocchia, A. Vigliani, Drivability enhancement and transient emission reduction for a mild hybrid diesel-electric truck, International Journal of Powertrains 2 (2013) 262–291, https://doi.org/10.1504/IJPT.2013.054154.

[48] A. Scamarcio, P. Gruber, S. De Pinto, A. Sorniotti, Anti-jerk controllers for automotive applications: A review, Annu Rev. Control 50 (2021) 174–189, https://doi.org/10.1016/j.arcontrol.2020.04.013.

[49] V. Ivanov, D. Savitski, B. Shyrokau, A Survey of Traction Control and Antilock Braking Systems of Full Electric Vehicles with Individually Controlled Electric Motors, IEEe Trans. Veh. Technol. 64 (9) (2015) 3878–3896, https://doi.org/10.1109/TVT.2014.2361860.

[50] A.J.C. Schmeitz, S. Jansen, H.B. Pacejka, J.C. Davis, N.N. Kota, C.G. Liang, G. Lodewijks, Application of a semi-empirical dynamic tyre model for rolling over arbitrary road profiles, International Journal of Vehicle Design 36 (2-3) (2004) 194–215, https://doi.org/10.1504/IJVD.2004.005356.

[51] Pacejka, H.B. (2012). *Tire and Vehicle Dynamics (Third Edition)*. https://doi.org/10.1016/B978-0-08-097016-5.02001-5.

[52] C. Lv, J. Zhang, Y. Li, Y. Yuan, Mode-switching-based active control of powertrain system with nonlinear backlash and flexibility for electric vehicle during regenerative deceleration, Proceedings of the Institution of Mechanical Engineers Part D Journal of Automobile Engineering 229 (2015) 1429–1442, https://doi.org/10.1177/0954407014563552.

[53] E. Galvagno, D. Morina, A. Sorniotti, M. Velardocchia, Drivability analysis of through-the-road-parallel hybrid vehicles, Meccanica 48 (2) (2013) 351–366, https://doi.org/10.1007/s11012-012-9606-6.

[54] R. Quirynen, M. Vukov, M. Zanon, M. Diehl, Autogenerating microsecond solvers for nonlinear MPC: A tutorial using ACADO integrators, Optimal Control Applications and Methods 36 (5) (2014) 685–704, https://doi.org/10.1002/oca.2152.

[55] G. Guastadisegni, S. De Pinto, D. Cancelli, S. Labianca, A. Gonzalez, P. Gruber, A. Sorniotti, Ride analysis tools for passenger cars: objective and subjective evaluation techniques and correlation processes – A review, Vehicle Syst. Dyn. (2023) 1–27, https://doi.org/10.1080/00423114.2023.2259024.

[56] H. Wang, B. Liu, X. Ping, Q An, Path Tracking Control for Autonomous Vehicles Based on an Improved MPC, IEEe Access. 7 (2019) 161064–161073, https://doi.org/10.1109/ACCESS.2019.2944894.

[57] H. Wang, Q. Wang, W. Chen, L. Zhao, D Tan, A novel path tracking approach considering safety of the intended functionality for autonomous vehicles, Proceedings of the Institution of Mechanical Engineers, Part D: Journal of Automobile Engineering 236 (4) (2021) 738–752, https://doi.org/10.1177/09544070211020535.

[58] P. Templin, Simultaneous estimation of driveline dynamics and backlash size for control design, in: IEEE International Conference on Control Applications, San Antonio, TX, USA, 2008, pp. 13–18, https://doi.org/10.1109/CCA.2008.4629642.

[59] P. Reddy, M. Shahbakhti, M. Ravichandran, J. Doering, Real-Time Estimation of Backlash Size in Automotive Drivetrains, IEEE/ASME Transactions on Mechatronics 27 (5) (2022) 3362–3372, https://doi.org/10.1109/TMECH.2021.3137461.

[60] ISO 8608:2016, Mechanical vibration, Road surface profiles.

[61] P. Múčka, Simulated Road Profiles According to ISO 8608 in Vibration Analysis, J. Test. Eval. 46 (2018), https://doi.org/10.1520/JTE20160265.